

Georgian Technical University

Faculty of Informatics and Control Systems

**Readout Upgrade for the Focal Plane Detector
of the Jülich Bragg Spectrometer**

Master Thesis of

Malkhaz Jabua

Head of Faculty Prof. Z. Tsveraidze

Advisers, Jülich Prof. D. Gotta
 Dr. H. Gorke

Adviser, Tbilisi Prof. L. Imnaishvili

Masters work carried out at the
Institut für Kernphysik
Forschungszentrum Jülich GmbH, Germany
2011

Contents

1	Introduction	5
2	X-ray spectroscopy using crystal spectrometers	6
2.1	Bragg law	8
2.2	Curved crystal spectrometers.	11
2.3	Jülich spectrometer	14
3	X-ray detectors	17
3.1	Different kinds of detectors for different purposes	17
3.2	Detectors types	17
3.3	CCD detectors	18
3.4	CCD architecture and charge storage	20
3.5	CCDs for X-rays	21
3.6	CCD X-ray energy resolution	26
4	Detector setup	27
4.1	CCD mounting	32
4.2	General structure of readout	33
4.3	Temperature control	35
4.4	CCD22 architecture	39
4.5	Detector operation overview	40
5	CCD readout and clock sequencing	42
5.1	Image integration	43
5.2	Frame transfer	43
5.3	Store region read-out	45
5.4	Readout scheme	47
5.5	How the sequencer timing is generated	49
5.6	ADC format for data digitization	52
5.7	ADC binary file readout	52
5.8	Results	53
6	Conclusion	56
A	Program Code to generate the timing sequence for the readout operation	57
B	Relationship between digital signals, memory bits and corresponding cabling pins.	63

List of Figures

1	Electronic transitions in an atom filling an inner shell vacancy.	6
2	Bremsstrahlung produced by an electron deflected in the electric field of an atomic nucleus.	7
3	Bragg reflection from crystal.	9
4	Bragg correction due to refraction.	10
5	Typical rocking curve for an ideal flat crystal	11
6	Schematic drawing of a Bragg spectrometer in Johann setup.	12
7	Setup of the Jülich spectrometer.	14
8	Quartz crystal on support lense.	15
9	Crystal support with crystal and aperture.	16
10	Bucket analogy used to describe CCD operation.	19
11	Typical CCD schematic.	20
12	Simplified buried channel CCD pixel structure.	21
13	Typical potential profile for buried channel CCD.	22
14	X-rays interacting with matter.	23
15	CCD22 quantum efficiency.	24
16	Metal-oxide-semiconductor structure on p-type silicon.	25
17	Standard 3-phase CCD structure.	26
18	CCD Cryostat setup.	27
19	Outer view of CCD cryostat.	29
20	CCD cryostat views.	31
21	Detector array prior to installation.	32
22	Structure of new readout.	34
23	outer distribution board used for readout operation from CCDs.	35
24	The whole ring of readout system	36
25	Inner temperature distribution board.	37
26	Installation of inner temperature distribution board	38
27	Temperature monitoring FIELDPOINT DAQ system.	39
28	location of temperature sensors.	40
29	outer temperature distribution board.	41
30	Connection between inner and outer temperature distribution boards.	42
31	Screen shot of the temperature monitoring panel of LABVIEW.	43
32	Internal structure of the software written in LABVIEW.	44
33	data file written by using LABVIEW, saving the temperature data.	45
34	CCD22 device schematic.	46
35	Typical clock and bias voltage requirements for a frame-transfer CCD.	47
36	Typical 3 phase, frame-transfer CCD schematic.	49
37	Frame transfer clock operation.	50
38	CCD output clock pattern.	51
39	Data format of CCD readout.	52
40	energy spectrum for CCD1 and CCD3 when the source ^{55}Fe is at 10 cm distance from the detector's sensitive surface.	55
41	energy spectrum for CCD1 and CCD3 when the source ^{55}Fe is at 20 cm distance from the detector's sensitive surface.	56

42	energy spectrum for CCD1 and CCD3 without ^{55}Fe	57
43	energy calibration for CCD1 and CCD3 when the source ^{55}Fe is at 10 cm distance from the detector's sensitive surface.	59
44	energy calibration for CCD1 and CCD3 when the source ^{55}Fe is at 20 cm distance from the detector's sensitive surface.	60

List of Tables

1	CCD optimised operating voltages.	48
2	parameters of energy spectra of the ^{55}Fe radioactive source.	54
3	Energies for $K\alpha$ (input) and $K\beta$ (prediction).	58
4	Relation between digital signals, memory bits and corresponding cabling pins. .	63
5	Relationship between digital signals, supply voltages and inner and outer distribution board connector pins.	64

1 Introduction

High resolution X-ray spectroscopy offers a powerful tool to study the complex electron-electron interaction in the atomic shells. The result may be confronted with modern theories describing such a many-body interactions. Experimentally, this requires an energy resolution of the order of one electron volt (eV) or better, which is achievable only with crystal spectrometers in the few keV range [1, 2].

Crystal spectrometry in this energy range exploits the so called Bragg law, which measures a wavelength precisely via a diffraction angle. The X-rays, analyzed by the Bragg crystal are recorded in nowadays sophisticated semiconductor devices like charge coupled devices (CCDs).

The work presented here, is embedded in a measurement series, which aims among others to investigate the L-shell structure and measure X-ray energy from Barium compounds (Ba_3N_2 , *Ba metal*, *Ba vapour*) [3].

The readout developed for the X-ray detector to be used in these experiments is adapted from a system developed for fast readout capable CCDs [4]. It allows a significantly improved readout performance and reliability.

Chapter 2 discusses the underlying physics principles of experiment, the nature of X-rays, Bragg diffraction in crystals, flat and spherically bent crystal features and other useful information which is important to understand the idea of experiment.

Chapter 3 contains information about detectors types, in particular for charge-coupled devices (CCDs), their working principle, physical processes inside the detectors, importance of the depletion layer, as well as energy resolution.

Chapter 4 discusses the CCD detector setup in detail, the arrangement of the hardware and electronic parts, and their parameters. It contains a detailed description of old and new readout system, their advantages and disadvantages and the temperature monitoring aspects.

In chapter 5, the timing sequences for the CCD readout are shown. The principles of data acquisition are explained. The advantage of using frame transfer CCDs is discussed, and the timing signals, analog-to-digital converter working principle and binary file readout formats are introduced. This chapter contains the main results of experiment. Energy spectra obtained with an ^{55}Fe radioactive source and energy calibration processes are described.

Chapter 6 is conclusion of the whole work.

2 X-ray spectroscopy using crystal spectrometers

X-rays are a form of electromagnetic radiation having wavelengths in the range of about 0.01 to 10 nanometers corresponding to frequencies in the range of 30 petahertz to 30 exahertz ($3 \cdot 10^{16}$ Hz to $3 \cdot 10^{19}$ Hz) or energies in the range of 120 eV to 120 keV. X-rays are shorter in wavelength than ultraviolet light and longer than gamma rays. In many languages, X-radiation is called Röntgen radiation, after Wilhelm Conrad Röntgen, who is generally credited as its discoverer, and who had named it X-radiation to signify an unknown type of radiation [5].

X-rays are emitted after vacancy production in the electron shell or as bremsstrahlung when charged particles are decelerated. They can be generated by an X-ray tube, where a high voltage accelerates electrons released from a hot cathode to a high velocity. The high velocity electrons collide with a metal target, the anode, creating there the X-rays. Typical high voltages are 30 to 150 kilovolts (kV). The X-ray spectrum depends on the anode material and the accelerating voltage.

The maximum energy of the produced X-ray photon is limited by the energy of the incident electron, which is equal to the voltage of the tube, so an 80 kV tube cannot create X-rays from bremsstrahlung with an energy greater than 80 keV.

As mentioned, when the electrons hit the target, X-rays are created by two different atomic processes:

1. X-ray fluorescence: If the electron has enough energy it can knock out an orbital electron of the inner electron shell of an atom, and as a result electrons from higher energy levels then fill up the vacancy and photons are emitted. This process produces an emission spectrum of X-rays at a few discrete frequencies. The energy of these spectral lines depend on the target (anode) element and thus are called characteristic lines [5]. In most cases, these are transitions from outer shells filling K hole (called K lines), a L hole (called L lines) and so on.

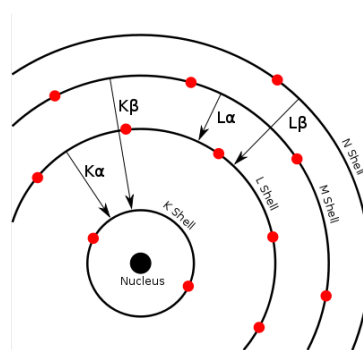


Figure 1: Electronic transitions in an atom filling an inner shell vacancy.

2. Bremsstrahlung: (german word from bremsen "to brake" and Strahlung "radiation", i.e. "braking radiation" or "deceleration radiation") is electromagnetic radiation produced by the deceleration of a charged particle when deflected by another charged particle, typically an electron by an atomic nucleus. The moving particle loses kinetic energy, which is converted into a photon because energy is conserved. Bremsstrahlung has a continuous spectrum being approximately proportional to $\frac{1}{E}$, which becomes more intense and is shifted towards higher frequencies when the energy of the accelerated particles increases [6].

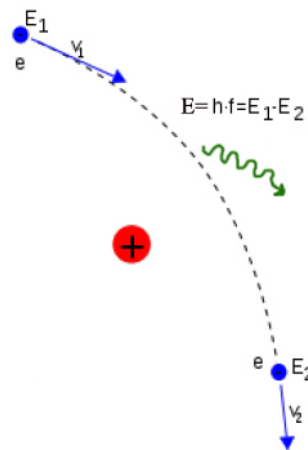


Figure 2: Bremsstrahlung produced by an electron deflected in the electric field of an atomic nucleus.

Here $E = h \cdot \nu$ is the Planck relation between the energy (E) of a photon and the frequency of its associated electromagnetic wave (ν), h is the Plank constant $4.1356 \cdot 10^{-15}$ in units of $\text{eV} \cdot \text{s}$.

X-rays from about 0.12 to 12 keV (10 to 0.10 nm wavelength) are classified as "soft" X-rays, and from about 12 to 120 keV (0.10 to 0.01 nm wavelength) as "hard" X-rays, due to their penetrating abilities.

"Hard" X-rays can penetrate solid objects, and their most common use is to take images of the inside of objects in diagnostic radiography and crystallography. As a result, the term X-ray is metonymically used to refer to a radiographic image produced using this method, in addition to the method itself. By contrast, "soft" X-rays hardly penetrate matter at all; the attenuation length of 600 eV (2 nm) X-rays in water is less than 1 micrometer.

2.1 Bragg law

The diffraction of X-rays by crystals was discovered by von Laue and his collaborators in 1912 [7]. This discovery resulted in the development of two complementary areas of research, the study of crystal structure using X-rays and the means of studying X-ray spectra to high precision using crystals. An estimation of the wavelength of X-rays already existed and von Laue calculated that the atomic spacing in a solid was of comparable dimension. He considered that a crystal may act like a diffraction grating and, consequently, tried to pass a narrow beam of X-rays through a zinc blende crystal, resulting in a pattern of diffraction spots on a photographic plate.

It was Bragg, who offered a simple interpretation of the diffraction patterns produced by von Laue. He suggested that each of the spots surrounding the central image could be a reflection of the X-ray beam from internal planes, within the crystal, that contains many regularly spaced atoms. Such planes should be parallel to the cleavage line of a crystal and Bragg tried reflecting an X-ray beam from such a surface of a mica crystal and using a photographic plate he recorded a spot at a specific angle of reflection.

Bragg reflection can be explained by considering the crystal structure as a regular array of identical planes of atoms, separated by a distance d , known as the lattice “ d -spacing”. An X-ray beam incident upon this crystal will be scattered by electrons of the regularly spaced atoms in the crystal producing a diffraction pattern. From the diagram we can see that the reflection path length difference between adjacent layers is equal to $AB + BC$, where $AB = BC = d\sin\theta_B$, (see Fig. 3). Constructive interference from diffraction from different planes of atoms will only occur when the path length difference is equal to an integral number of wavelengths of the incident X-ray beam. This is known as Bragg’s law and can be stated as:

$$n\lambda = 2d\sin\theta_B, \quad (1)$$

where n is the order of diffraction, λ - the wavelength of the radiation, d is the crystal d -spacing and θ_B is the angle of Bragg reflection or Bragg angle [8].

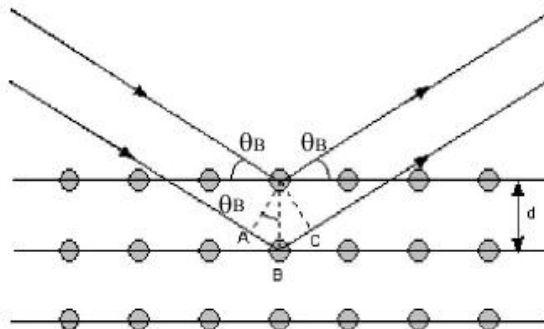


Figure 3: Bragg reflection from crystal.

This relation between refraction angle and wavelength is used in spectroscopy to transform an energy in an angle measurement, by using the relation $E = hc/\lambda$ with c being the speed of light in vacuum.

An important correction to Bragg's law stems from the index of refraction of the crystal material. For X-rays the refractive index is less than 1 and so the X-ray path is bent away from the normal inside the crystal (see Fig. 4). This alters the extra distance traveled by X-rays reflected from each "lower" plane of atoms and consequently changes the path difference for the Bragg condition to occur.

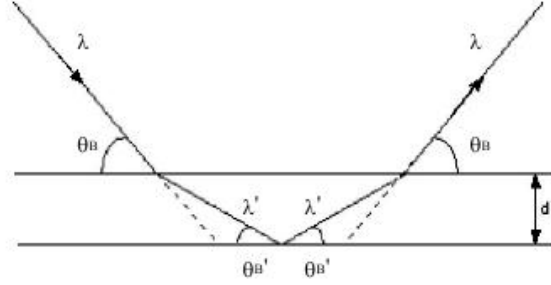


Figure 4: Bragg correction due to refraction.

The refraction index μ is parametrised (neglecting absorption) as

$$\mu = 1 - \delta, \quad (2)$$

with δ being a small positive number. Inside the crystal, the X-ray wavelength changes from λ to λ' , the angle for Bragg reflection becomes θ_B' . Considering the refraction at the crystal surface due to Bragg's law and rewriting it inside the crystal leads to

$$n\lambda' = 2d\sin\theta_B'. \quad (3)$$

One obtains [9]

$$\mu = 1 - \delta = \frac{\lambda}{\lambda'} = \frac{\cos\theta_B}{\cos\theta_B'}. \quad (4)$$

Eliminating μ and primed variables leads to

$$n\lambda = 2d\sin\theta_B \left(1 - \frac{2\delta - \delta^2}{\sin^2\theta_B} \right)^{\frac{1}{2}}. \quad (5)$$

Since δ is of order 10^{-6} , we can ignore δ^2 , expand the bracket and, again ignoring powers of δ higher than 1 and get

$$n\lambda = 2d\sin\theta \left(1 - \frac{4d^2}{n^2 \cdot \lambda^2} \delta \right), \quad (6)$$

which is known as the modified Bragg law [10].

The correction factor in brackets (6) varies with order of reflection becoming less significant as the order increases. Hence, the diffraction Bragg angle θ' differs from the uncorrected Bragg angle θ_B by an amount $\Delta\theta_{ind}$ usually expressed as

$$\theta' = \theta_B + \Delta\theta_{ind}. \quad (7)$$

The intrinsic properties of single crystals can be calculated to within a few percent by dynamical theory of diffraction [11]. The most important parameters are the crystal rocking curve width ω , the peak reflectivity P and the integrated reflectivity R_I (see Fig. 5).

The rocking curve width ω describes the divergence of a parallel, monoenergetic beam of radiation after Bragg reflection by the crystal. The peak reflectivity P represents the maximum reflected intensity in the diffraction profile and takes into account incoherent factors such as photon absorption.

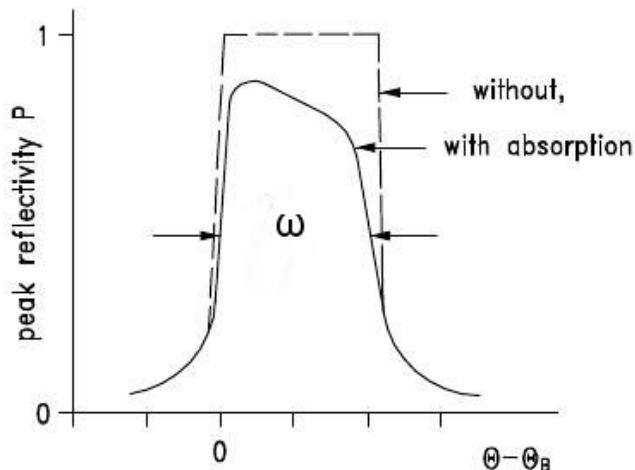


Figure 5: Typical rocking curve for an ideal flat crystal

The integrated reflectivity R_I is a measure of the total intensity of the reflected radiation and is related to ω and P by

$$R_I \approx \frac{4}{3} P \omega \quad (8)$$

where R_I and ω are usually given in radians. Here we see that when the resolution increases (ω decreases) the integrated reflectivity or count rate decreases [12].

As described above the Bragg condition is only fulfilled for a small angular interval ω leading to a low rate of reflected X-rays coming from a spatially extended source. To increase the efficiency, i.e., increasing the rate of reflected X-rays, focusing spectrometers with cylindrically or, like in this experiment, spherically bent crystals are used [3, 13]. Common are reflection-type spectrometers of the so called Johann geometry.

2.2 Curved crystal spectrometers.

In the Johann setup an extended source, a bent crystal and a detector are placed on the so-called Rowland circle [14] (see Fig. 6). The radius of the Rowland circle (R) is equal to half of the bending radius of the crystal R_c . The focusing condition for a beam hitting the crystal at the very center is

$$Y = R_c \cdot \sin \theta_B \quad (9)$$

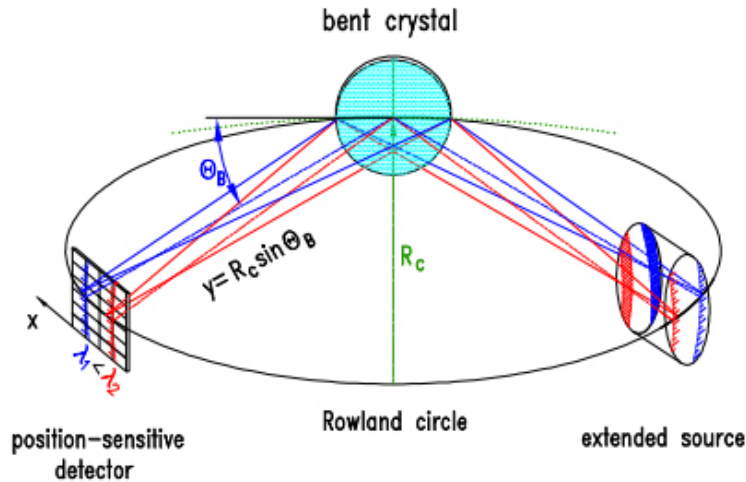


Figure 6: Schematic drawing of a Bragg spectrometer in Johann setup. This setup together with an extended source and detector allows for simultaneous measurement of a finite energy interval. Smaller wave lengths (higher energies) belong to smaller Bragg angles θ_B .

Using this setup an extended source together with a large-area detector allows for a simultaneous measurement of an energy interval given by the horizontal extension of source and/or detector. X-rays with different wave lengths are accepted from different places of the extended source and are focused to adjacent places on the detector. In that way the position spectrum measured in the detector plane contains information about the energy differences of the diffracted X-rays. This relation can be expressed as equation of the local dispersion [3]

$$\frac{dE}{dx} = \frac{E}{R_c \cdot \sin \theta_B \cdot \tan \theta_B} \quad (10)$$

with the direction x of the local dispersion perpendicular to the axis crystal-detector (see Fig. 6).

Usually this setup is modified such, that the extended source is placed about 20% off the focal distance inside the Rowland circle. In this way, non uniformities of the source are averaged out, because now not only X-rays from one narrow strip, but from a large region of the source fulfil the Bragg condition. Placing the source outside the Rowland circle results in the same affect, but reduces the effective source width and, therefore, the size of the measurable energy interval.

The different radii of the crystal and the Rowland circle lead to a defocussing of the parts of the beam that are not reflected at the center of the crystal and,

thus, cause a broadening of the measured X-ray line. From geometrical considerations it can be seen, that X-rays not hitting this central ray to the crystal are always reflected to the high energy side, i.e., towards smaller Bragg angles. This shift is maximal at the edges of the crystal. At this point, assuming the total horizontal width of the crystal to be b , in the symmetry plane the so called Johann shift reads in leading order [14]

$$\Delta\theta_J = \frac{1}{2} \left(\frac{b}{2R_c} \right)^2 \cot\theta_B \quad (11)$$

The Johann broadening can be tolerated if it is small compared to the intrinsic crystal resolution, which is the case for a large crystal bending radius R_c . An aperture in front of the crystal width can be used to limit the broadening.

In principle one can avoid this geometrical aberration using the Johansson setup [3]. There the crystal is again bent to a radius equal to two times the radius of the Rowland circle as it is the case in the Johann setup, but additionally the crystal surface is ground with the radius of the Rowland circle. In this way, the crystal surface is always at the Rowland circle. In practice, this is realised for compact industrial spectrometers of moderate resolution. The production of such crystals for large bending radii of three meters was not necessary for this experiment because resolutions close to the theoretical limit are achievable also with the Johann setup.

The bending of the crystal not only in the horizontal but also in the vertical direction increases the efficiency of the spectrometer, because the additional vertical focusing reduces the reflection height and, hence, enlarges the hit density at the detector. The crystal expansion in vertical direction leads to a curvature of the reflection in direction to lower energies which can be measured by a two-dimensional position-sensitive detector.

2.3 Jülich spectrometer

Figure 7 shows the setup of the Jülich crystal spectrometer working according to the principle shown in Figure 6. Details can be found in [3, 13].

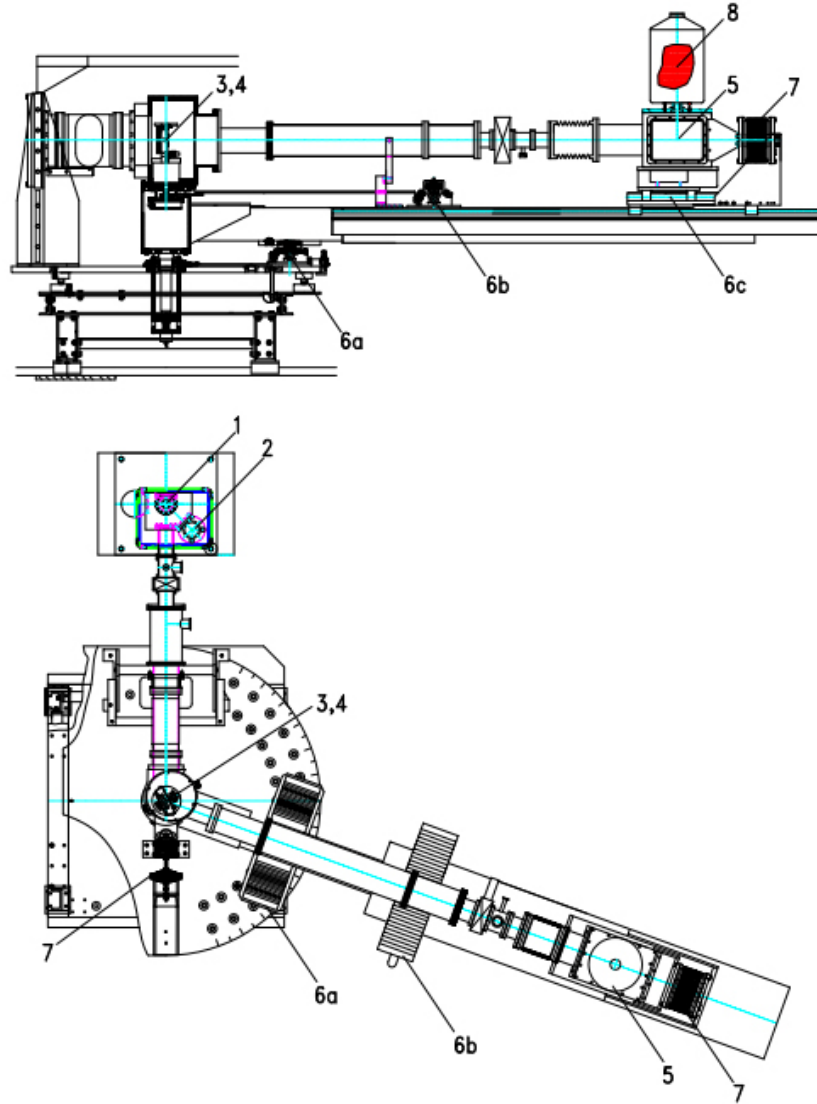


Figure 7: top - side view of the detector arm, bottom - top view. 1: position of fluorescence target, 2: X-ray tube, 3,4: Bragg crystal, support, 5: detector cryostat, 6: linear tables for a) arm, b) crystal and c) detector movements, 7: traction relaxation, 8: LN_2 -dewar. (From [3, 13]).

X-rays generated by an X-ray tube and diffracted by Bragg crystal hit the X-ray detector (5) [3].

To meet the dimensional requirements of the detector, an array of X-ray sensitive CCDs is located at the focus of the spectrometer. All parts of the setup are connected by vacuum tubes to prevent absorption of the few keV X-rays. For safety reasons, the system is divided into two independent parts. The detector chamber is evacuated to a pressure of approx. $2 \cdot 10^{-7}$ mbar with a combination of

a membrane and a turbomolecular pump.



Figure 8: Quartz crystal on support lens.

As an example for a Bragg crystal mounting, a quartz crystal is shown in Figure 8. The mounting is produced in cooperation with the company Carl Zeiss in Oberkochen, Germany. The quartz crystal is of $200\ \mu\text{m}$ thickness and $100\ \text{mm}$ in diameter and attached on a $30\ \text{mm}$ thick spherically polished glass lens of $120\ \text{mm}$ in diameter. The crystal is cut parallel to the $(1\ 0\ -1)$ lattice plane. The bending radius of the lens is $2982.5\ \text{mm}$.

The crystal, mounted on the glass lens, is placed in a support which allows for precise vertical positioning of the reflexion. This is achieved by a direct current motor, that inclines the crystal through the horizontal axis (see Fig. 9).

An aperture with a size of 60 mm horizontally and 95 mm circularly is placed in front of the crystal in order to limit the Johann-broadening.



Figure 9: Crystal support with crystal and aperture of 60 mm width. On the bottom left side the servomotor with linear potentiometer for tilting of the mirror is shown (from [3]).

The X-ray detector is discussed in detail in chapter 3.

3 X-ray detectors

3.1 Different kinds of detectors for different purposes

A principal question when selecting a detector for a given application is to determine exactly the need for the envisaged measurements. One can try to get an image of the X-ray source by recording detailed position information of the incoming light or measure its energy spectrum, which requires getting a very accurate measurement of the energy of each incoming X-ray or to get timing information by measuring the arrival time for incoming photon. Finally, to achieve sufficient count rates, a suitably large detector size has to be chosen. An ideal detector fulfills all the features, but in practice, detectors are optimized for one quantity and then have less accuracy in determining the remaining ones.

In the case discussed here, the energy determination is performed at ultimate precision by using Bragg diffraction (chapter 2). The X-ray detector itself serves for identifying the X-rays and to measure the impact coordinates.

3.2 Detectors types

There are three main designs for X-ray detectors: gas-filled detectors, scintillation counters, and semiconductor detectors. In all of these designs, an incoming low-energy X-ray produces a photo electron when interacting with the material of the detector. In this photoelectric effect, electrons are emitted from atoms as a consequence of the absorption of energy from electromagnetic radiation. The photo electrons collide within the detector material and create ion-electron pairs until their kinetic energy is used up. The number of electron-ion pairs depends on the initial energy of the incident X-ray. The output of the detector can therefore be analyzed based on pulse height to obtain an energy spectrum of the incident radiation.

Gas-filled detectors consist of a container filled with a gas such as argon, a window that allows transmission of X-rays, such as beryllium or mylar, and one or more wires that serve as an anode. A high voltage is applied between a second electrode operated as cathode and the anode. When accelerated the photo electron ionizes more gas atoms. The released electrons are again accelerated thus providing by further ionisation an electron avalanche, which is collected by the anode and detected as an electrical pulse.

A scintillator is a material that emits light when it absorbs radiation. The light pulse is then converted to an electrical pulse by a photomultiplier tube. Common scintillators are thallium-doped NaI, some plastics, anthracene and other organic solids, and liquid scintillation "cocktails," which are mixed with the sample and are often used in biochemical applications. Because of the low light output such detectors are mainly used for higher energetic radiation like γ rays.

Semiconductor detectors are often used in high-energy physics for tracking usually in the form of strip detectors, because of their unmatched energy and spatial resolution and excellent response time. These detectors are manufactured mainly of silicon, traditionally on high-resistivity single crystal float-zone material. The principle of operation of a semiconductor detector is the following: if an

ionizing particle penetrates the detector it produces electron-hole pairs along its track, the number being proportional to the energy loss. An externally applied electric field separates the pairs before they recombine; electrons drift towards the anode, holes to the cathode, where the charge is collected. The collected charge produces a current pulse on the electrode, whose integral equals the total charge generated by the incident particle, i.e. is a measure of the deposited energy. The readout is performed through a charge-sensitive preamplifier, followed by a shaping amplifier [22].

The most common X-ray detectors use lithium-drifted silicon Si(Li) or lithium-drifted germanium Ge(Li). In these detectors, Li is incorporated into the semiconductor lattice by annealing the semiconductor with Li at a high temperature. A voltage of typically 1000 V is placed across the semiconductor material with two electrodes, and the charge produced by a photo electron is detected as an electrical pulse at the anode.

In addition to being more robust than gas-filled or scintillator detectors, these semiconductor detectors also provide a much better energy resolution. Their disadvantage is the need for cooling, usually with liquid nitrogen, to decrease the dark noise of the detector and current-to-voltage preamplifier to achieve reasonable energy resolution. In addition, they usually don't provide any two-dimensional position resolution as required for a Johann spectrometer [14].

3.3 CCD detectors

A charge-coupled device (CCD) is a device for the movement of electrical charge, usually from within the device to an area where the charge can be manipulated, for example amplified and converted into a digital value. This is achieved by shifting the collected charge between defined places within the device to an output electrode. CCD is a semiconductor detector, which provides a two-dimensional position resolution by its surface structure. The charge locally created, e.g. by a photo electron is kept in place by electric potentials allowing the reconstruction of the impact coordinates.

Basically, a CCD is a sensor for recording images. It consists of an integrated circuit containing an array of linked or coupled capacitors acting as many small pixels. The light falling on a pixel is converted into a charge pulse after digitization. Because of a dedicated surface structure the charge is captured in a pixel in a potential minimum. The more light falls on the pixel, the more charge will accumulate in the pixels until saturation is reached. The amount of charge is a measure of the amount of light arriving at the pixel which is read out by the CCD electronics and converted to an image.

The principle of CCD operation can be demonstrated as a "bucket brigade" (see Fig. 10). Here rain drops correspond to photons and buckets to pixels. Determination of the brightness distribution in a CCD image can be linked to measuring the rainfall at different points in a field with an array of buckets. Once the rain has stopped, the buckets in each row are moved down vertically across the field on conveyor belts. As the buckets in each column reach the end of the conveyor, they are emptied into another bucket system on a horizontal belt, that

carries it to a metering station where its contents are measured [15].

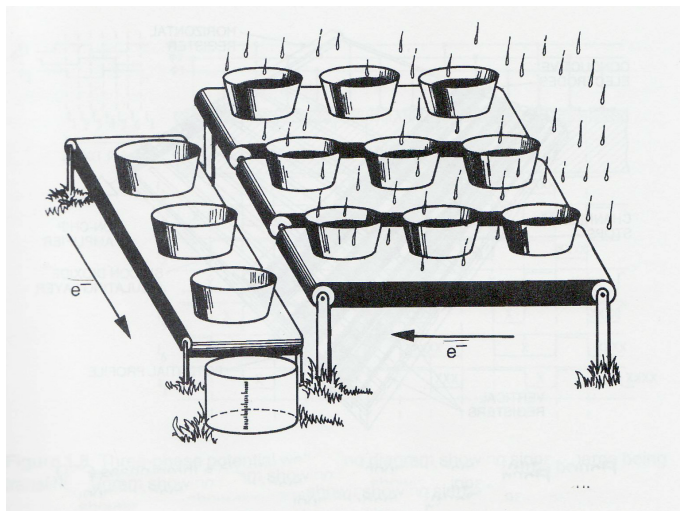


Figure 10: Bucket analogy used to describe CCD operation.

Often the device is integrated with an image sensor, such as a photoelectric device to produce the charge that is being read, thus making the CCD a major technology for digital imaging. Although CCDs are not the only technology to allow for light detection, CCDs are widely used in professional, medical, and scientific applications when high-quality image data are required.

In a CCD for taking images, there is a photoactive region (an epitaxial layer of silicon), and a transmission region made out of a shift register (the CCD, properly speaking). In case of a digital camera, an image is projected through a lens onto the capacitor array (the photoactive region), causing each capacitor to accumulate an electric charge proportional to the light intensity at that location. A one-dimensional array, used in line-scan cameras, captures a single slice of the image, while a two-dimensional array, used in video and still cameras, captures a two-dimensional picture corresponding to the scene projected onto the focal plane of the sensor. Once the array has been exposed to the image, a control circuit causes each capacitor to transfer its contents to its neighbor (operating as a shift register). The last capacitor in the array dumps its charge into a charge amplifier, which converts the charge into a voltage. By repeating this process, the controlling circuit converts the entire contents of the array in the semiconductor pixel by pixel to a sequence of voltages. In a digital device (e.g., a digital camera), these voltages are then sampled, digitized and stored.

3.4 CCD architecture and charge storage

A charge-coupled device is usually fabricated from p -type silicon. It comprises an array (either one or two dimensional) of elements or pixels capable of storing local, photon generated charge. A general scheme for CCD is shown in Fig. 11. It consists of an image and a line readout section.

The stored charge is then shifted one row at a time into the line readout section and each pixel is then moved sequentially towards an output node and measured.



Figure 11: Typical CCD schematic.

In this way, a charge map or image of the whole CCD can be constructed.

The storage elements of CCDs are essentially an array of metal-oxide-semiconductor (MOS) capacitors. The capacitors comprise a conducting electrode deposited onto the silicon substrate with a thin insulating layer of silicon dioxide between. Each pixel actually contains a coupled number of MOS capacitors, commonly three (see Fig. 12).

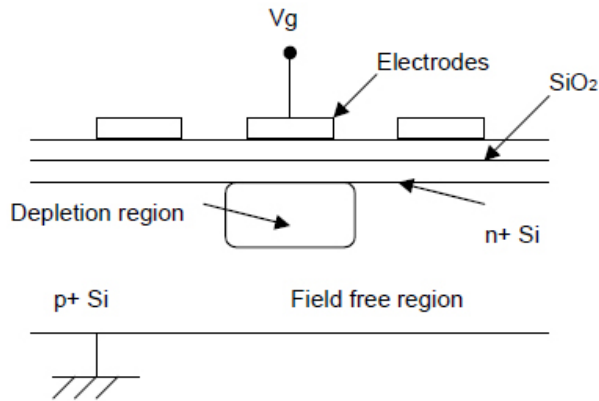


Figure 12: Simplified buried channel CCD pixel structure.

Application of a positive voltage to one of the conducting electrodes or gates, will create a region depleted of holes beneath the electrode. The n+ silicon layer modifies the shape of the electrostatic potential profile of this depletion region, creating a "buried channel", which allows charge collection away from the surface, where the trapping sites would reduce the charge collection and transfer efficiency.

The electrostatic potential profile, in terms of variation of electric field with depth in the silicon, can be derived using Poisson's equation (12) [16]

$$\frac{d^2V}{dx^2} = \frac{e(N_d^+(x) - N_a^-(x) - n(x) + p(x))}{\epsilon_{Si}\epsilon_0}, \quad (12)$$

where e is the unit of electric charge, N_d^+ is the donor concentration in the p+

silicon, N_a^- is the acceptor concentration in the n+ silicon, n and p are the number of thermally generated electrons and holes and ϵ_{Si} and ϵ_0 are the permittivities of silicon and free space. This equation can be solved numerically and Fig .13 shows a potential profile for a buried channel CCD using typical dopant concentrations [15].

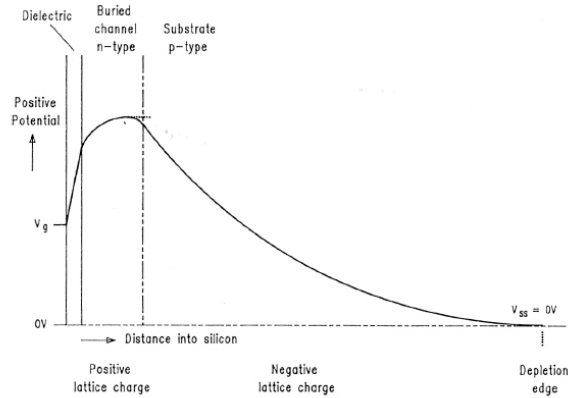


Figure 13: Typical potential profile for buried channel CCD.

CCDs were initially conceived to operate as a memory device as an electronic analog of magnetic bubble device. In order to function as memory, there must be a physical quantity that represents a bit of information, a means of recognizing the presence or absence of the bit (reading) and a means of creating and destroying the information (writing and erasing). In a CCD, a bit of information is presented by a packet of charges. These charges are stored in the depletion region of the metal-oxide-semiconductor (MOS) capacitor.

Charges are moved about the CCD circuit by placing MOS capacitors very close to each other and manipulating voltages on the gates of the capacitors. In this way the charge spills from one capacitor to the next (see chapter 5). Thus the name charge-coupled device.

3.5 CCDs for X-rays

When using CCD detectors for X-ray measurement, they have advantages over other X-ray detectors:

1. Intrinsic spatial resolution for low-energy X-radiation in two dimensions.
2. Good resolution of the collected charge as usual for semiconductor detectors.
3. Pattern recognition allows background suppression in particular in accelerator environments.
4. High quantum efficiency (QE). It is defined as the ratio of number of X-rays detected to number of incident X-rays and is expressed either as a value between 0 and 1 or as a percentage.

5. Good level of linearity. Linearity is a measure of how consistently the CCD responds to light over its well depth. For example, if a 1-second exposure to a stable light source produces 1000 electrons of charge, 10 seconds should produce 10,000 electrons of charge. The deviation from this straight line is a measure of non-linearity.
6. In contrast of optical CCD devices X-ray detectors are supposed to detect single photons, where energies are of several orders of magnitude higher than for visible light.

The key feature which makes these devices effective X-ray sensors and allows the determination of the photon energy is an enlarged depleted layer of silicon near the surface.

In semiconductor physics, the depletion region, also called depletion layer, is an insulating region within a conductive doped semiconductor material where the mobile charge carriers have diffused, driven away by an electric field. The only elements left in the depletion region are ionized donor or acceptor impurities.

When the photo electron interacts with the silicon lattice of the detector a cloud of electrons and holes is created. If the interaction occurs in the depletion layer, all electrons will be pulled by the electric field and collected in the potential well underneath the gates.

The depletion depth determines the high-energy detection limit of the CCDs. Therefore charge-coupled devices fabricated on high resistivity substrates are becoming increasingly popular.

The depletion layer thickness is the parameter that determines the quantum efficiency of CCD detector. The high energy detection limit of the X-ray CCD is of major importance for X-ray detection. The depletion depth is the main difference between X-ray CCD detectors and other CCDs. Optical CCD detectors have depletion depths of less than $5 \mu m$, that's why they are inefficient in X-ray detection above 2 keV.

When X-rays interact with matter, they are partly absorbed and partly transmitted. The intensity of a photon beam decreases according to:

$$I = I_o e^{-\mu x}, \quad (13)$$

where I is the transmitted beam intensity, I_o the incident beam intensity, μ the linear absorption coefficient, e is Euler's number, and x the thickness of the material (Fig. 14).

The linear absorption and mass absorption coefficients (α) are related by $\alpha = \frac{\mu}{\rho}$, where ρ is the density of the material.

The transmission of a photon beam is given by

$$T = \frac{I}{I_o} = e^{-\mu x} \quad (14)$$

and consequently the absorbed fraction is

$$A = \frac{I_o - I}{I_o} = 1 - e^{-\mu x}. \quad (15)$$

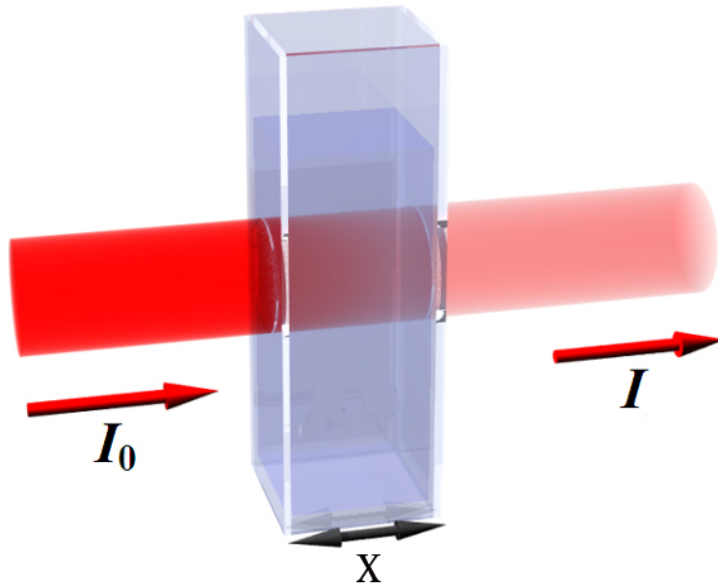


Figure 14: X-rays interacting with matter.

Figure 15 displays the quantum efficiency of a CCD as used in this experiment in the range of 1-10 keV [16]. The solid line is a simple analytical model using the absorption depth of photons in silicon combined with absorption in the overlying electrode structure and associated layers.

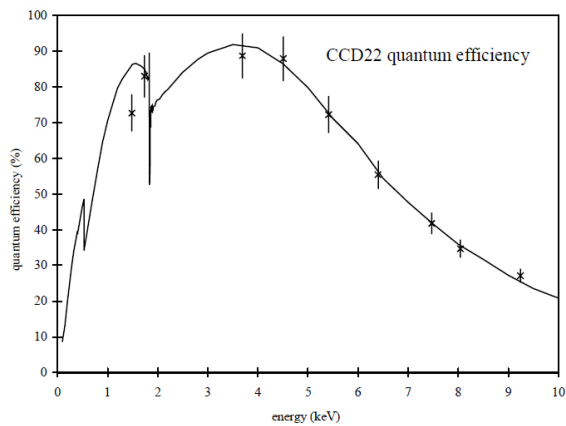


Figure 15: CCD22 quantum efficiency. (From [16]).

Because of the short range of photo electron, the signal charge is either confined within one pixel (this is called a single pixel event), or split between two adjacent pixels horizontally or vertically. Large configurations (for instance, a four-pixel event) occur for higher energetic X-rays converting at the boundary of the depletion region which leads to diffusion of the charge cloud. If all the pixels containing the signal charge are summed together, the amplitude of the sum corresponds to the total energy of the incident photon [17].

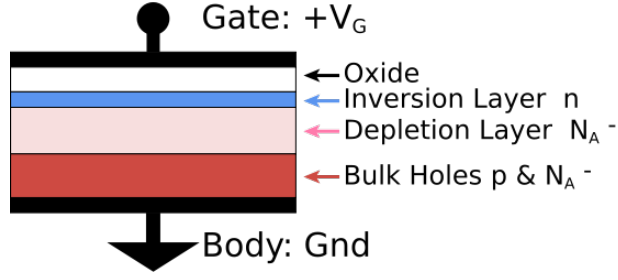


Figure 16: Metal-oxide-semiconductor structure on p-type silicon.

The depletion region for a p-type substrate is shown in Figure 16. Supposing that the semiconductor initially is charge neutral, the charge due to holes exactly balances the negative charge due to acceptor impurities. If a positive voltage is applied to the gate, which introduces positive charge Q to the gate, then some positively charged holes in the semiconductor nearest the gate are repelled by the positive charge on the gate, and exit the device through the bottom contact. They leave behind an enlarged depleted region that is insulating because no mobile holes remain, but only the immobile, negatively charged acceptor impurities. The greater the positive charge placed on the gate, i.e., the higher the positive gate voltage, the more holes leave the semiconductor surface and enlarge the depletion region. In this device there is a limit on the depth of the depletion layer. It is set by the onset of an inversion layer of carriers in a thin layer, or channel, near the surface. The above discussion applies for positive voltages low enough that an inversion layer does not form.

The depletion depth can be measured according to this formula [17]:

$$d_d = \tau \ln \frac{N_d}{N_{und}} + 1 \quad (16)$$

N_d is the number of interactions in the depleted region and N_{und} the number of events in the undepleted bulk, τ is characteristic absorption length used for the X-ray photons.

A standard CCD is typically manufactured from low-resistivity ($50 \Omega\text{cm}$) $25 \mu\text{m}$ epitaxial silicon on a $550 \mu\text{m}$ p+ silicon substrate (see Fig. 17).

The epitaxial silicon surface is passivated, first with a $0.1 \mu\text{m}$ layer of silicon dioxide and then with a similar thickness of silicon nitride. On top of the passivation layers are the three electrodes, constructed by depositing n -type polycrystalline silicon (polysilicon) with an insulating layer of silicon dioxide between electrodes. The electrodes overlap in the manner shown in Figure. 17 but are nominally of the same width $1/3$ pixel width, providing a similar depletion capability underneath each one. Finally, a vapour deposition of silicon dioxide (VAPOX) is applied to protect and passivate the CCD surface. When the gate potential is applied to the electrode, a typical depletion depth of $5 \mu\text{m}$ is achieved with a corresponding field-free region of $25 \mu\text{m}$.

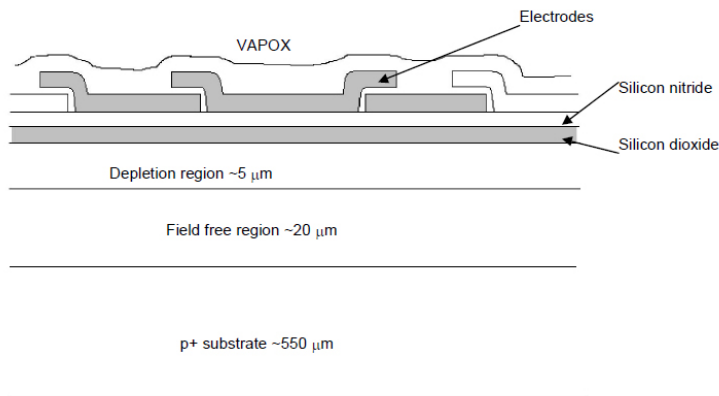


Figure 17: Standard 3-phase CCD structure.

For an X-ray to be detected by the CCD, it must interact in the epitaxial silicon and this process is affected by two areas of CCD design, (a) the electrode structure and (b) the epitaxial thickness. Charge generated in the electrode structure is not collected and essentially forms a $1.5 \mu\text{m}$ dead layer thick on the surface of the CCD. Absorption of X-rays in this layer determines the low energy response of the CCD. Charge collected in the $p+$ substrate diffuses and is lost, effectively limiting the high-energy response [15].

3.6 CCD X-ray energy resolution

The energy resolution of a CCD depends upon the collected charge statistics and internal and external noise sources. Noise sources are either signal related (shot noise, dark current) or device related (charge transfer losses, reset noise, output amplifier noise). The energy resolution can be expressed as

$$\Delta E(FWHM) = 2.355 \omega \left(\frac{F E_x}{\omega} + \sigma_T^2 \right)^{\frac{1}{2}}, \quad (17)$$

where the first term in the brackets is the Fano modified signal shot noise and σ_T is the total rms (root mean square) read noise of the CCD electronics.

E_x is the energy of the interacting photon and ω is the mean ionisation energy to create one electron-hole pair. The number of electron-hole pairs is given by $N = \frac{E_x}{\omega}$. Since some of the ionisation energy is lost to the crystal lattice (photons) ω is somewhat larger than the bandgap energy of silicon. N is a statistical quantity but, since the creation of electron-hole pairs is not mutually exclusive, the variation is less than that given by purely random statistics. The usual Poissonian variance is modified by an empirical quantity known as Fano factor, which is found to be $F = 0.15$ for silicon [23]. Ultimate resolution is achieved by minimising the noise terms associated with σ_T and in this case the detector performance is Fano limited.

4 Detector setup

The focal plane detector for the Jülich crystal spectrometer device is built up from an array of six high-resistivity individual CCDs. A large detection area is chosen because of the need to detect simultaneously two or more lines close in energy as well as broad structures like fluorescence X-rays from electronic atoms.

Figure 18 shows the hardware parts of mechanical setup and the connections between them.

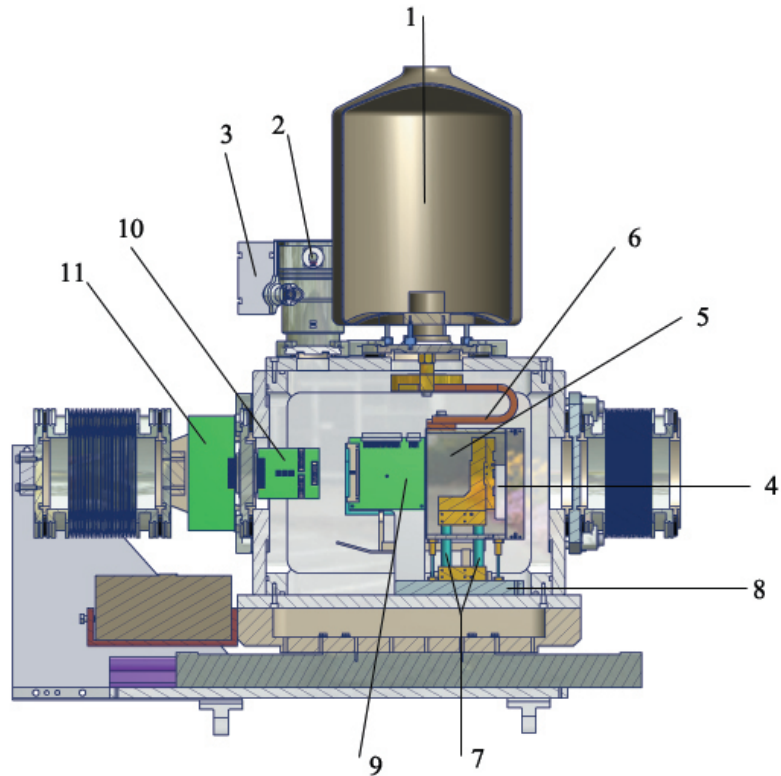


Figure 18: CCD Cryostat setup.

LN_2 dewar(1) used for cooling; Valve (2) allowing to disconnect the turbomolecular pump (3) without losing the cryostat vacuum; CCDs (4) are inside the aluminum shield (5), which acts as a cold trap; Connection (2 copper braids) (6) between the dewar and CCD mounting; (7) temperature insulation between CCDs and detector support (8); (9) temperature distribution board for the temperature sensors (PT 100); (10) distribution board for CCD timing signals and CCD bias voltages. It allows to transfer digital signals to the preamplifier boards and to receive the analog output [24]; (11) outer board connected to inner board by a 50 pin vacuum fieldthrough. The sequencer transfers the digital timing signals (see chapter 5) to this board. All voltages that are necessary for the CCDs are also connected to this board.

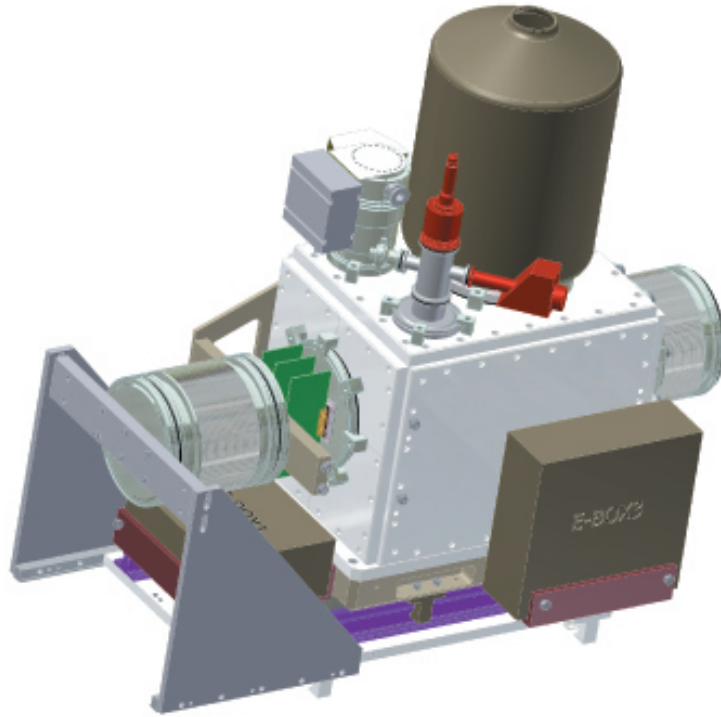


Figure 19: Outer view of CCD cryostat.

In order to read out the information correctly from CCDs, it is important to cool them down. A cold finger is cooled using liquid nitrogen and a closed-loop temperature control maintains the CCD temperature at $(-100 \pm 0.5 \text{ }^\circ\text{C})$ to reduce thermally generated dark current to negligible levels.

Dark current arises from thermal energy within the silicon lattice comprising the CCD. Electrons are created over time independent of the light falling on the detector. These electrons are captured by the CCDs potential wells and counted as signal. Additionally, this increase in signal also carries a statistical fluctuation known as dark current noise. CCDs can be cooled either with thermoelectric coolers (TECs) or liquid nitrogen to reduce this effect. Ideally, the dark current noise should be reduced to a point where its contribution is negligible over a typical exposure time.

The aluminum shield is cooled first by direct connection to the liquid nitrogen feed. In this way it acts as a cold trap for any remaining water or contaminants. The shield itself is wrapped by superinsulation (several layers of metalised Mylar) to reduce the heat load.

4.1 CCD mounting

The array comprises six CCD22 devices arranged as two columns of three. They have a sensitive area of $24\text{ mm} \times 24\text{ mm}$, each, yielding a total imaging area of $48\text{ mm} \times 72\text{ mm}$. Each CCD consists of 600×600 pixels and each pixel has a size of $40\ \mu\text{m}$. There is a maximum gap of $500\ \mu\text{m}$ between devices and they are rotationally aligned to better than 7 mrad [18].

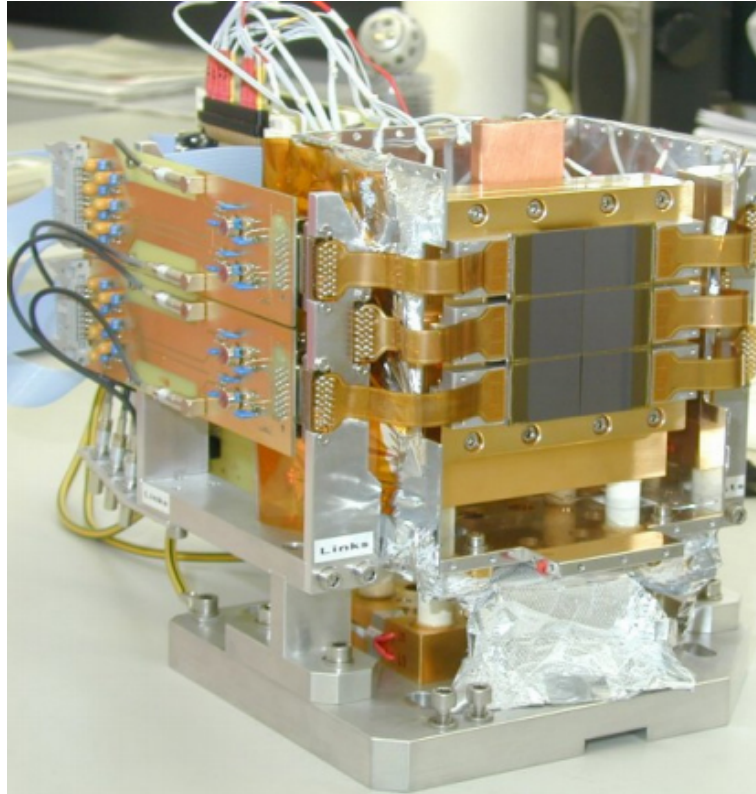


Figure 21: Photograph showing 2×3 CCD array mounted on cold-finger prior to installation inside vacuum cryostat. The total imaging area $48\text{mm} \times 72\text{mm}$.

The six CCDs are attached to an invar cold-finger and the whole assembly is mounted inside a custom built, stainless steel vacuum cryostat. Electrical connection is provided for the clock and bias signals via a Kapton flex-circuit.

4.2 General structure of readout

In the previous read out system the six CCD22 devices have been controlled by an IBM compatible PC running under windows 95 operating system. Programmable bias voltages and clock sequences were generated by two PC expansion cards. These signals were multiplexed in a separate clock driver device and transferred to the CCDs. The analog output has been processed by a 3-channel device using correlated double sampling technology (CDS) to minimise noise level.

The main disadvantage of this system is it's low level of reliability. Hardware resources which are used for readout operation also the ones for the operating parameters are located in a PC. So, if there is a problem with PC, the complete system stops. In addition, some of the expansion cards require the windows 95 operating system, being incompatible with nowadays standards.

In the new readout system the six CCD22 are controlled from a Linux based PC using a combination of custom and commercial electronics. The advantage of the new setup is flexibility and high level of reliability. It consists of da new etector cryostat (chamber), and front-end electronics, which has to be located close to the chamber. Data storage is performed at the Linux PC.

Figure 22 shows the general structure of front-end hardware parts. The front-end electronics is realised as one crate containing one module for optical pci bridge (for fiber optics connection), one for the sequencer unit and two analog-to-digital (ADC) units. PC and the crate are physically separated. This provides a high level of reliability, because in case of computer crash the front-end electronics continues to function, In this way risks connected to whole system functionality are minimised.

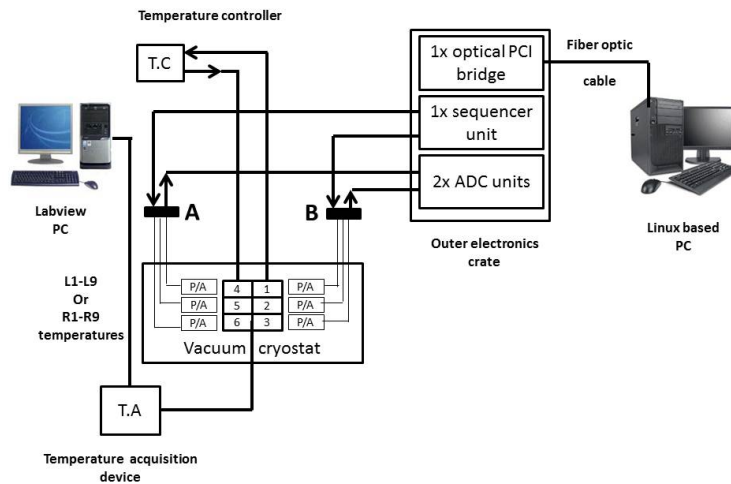


Figure 22: Structure of new readout.

Communication between PC and the front-end electronics crate is done by a fiber optic cable. On one hand this guarantees high speed connection and on the other hand allows to have full software control remotely.

Unlike in the previous readout system, signal multiplexing is no longer needed, because timing for every CCD is generated at the same time. For readout digital signals are transferred to the CCDs. Analog signals are received from the preamplifiers. A and B, which can be seen in Figure 22, represent the boards used for distributing this signals to CCDs. Directions are indicated by up and down arrows. One of these boards is shown in Figure 23. Analog output from the preamplifiers must be amplified. Amplification and correlated double sampling is done by a separate amplifier device, from which the signals are fed to ADC units, where they are converted to digital values [24]. Each ADC unit works with 3 CCDs. The readout procedure from all CCDs is synchronised, so the data transfer of all of them occurs simultaneously.

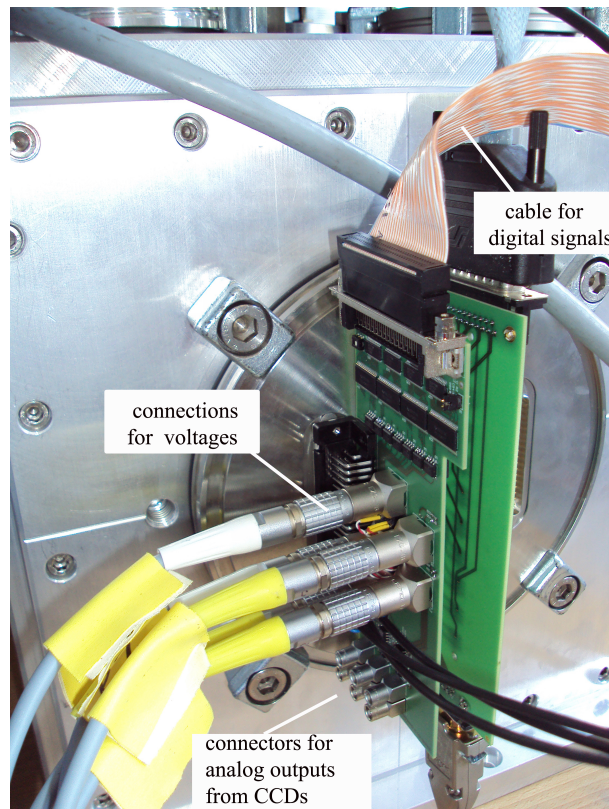


Figure 23: outer distribution board used for readout operation from CCDs.

Connection between the sequencer and outer board can be seen in Figure 24.

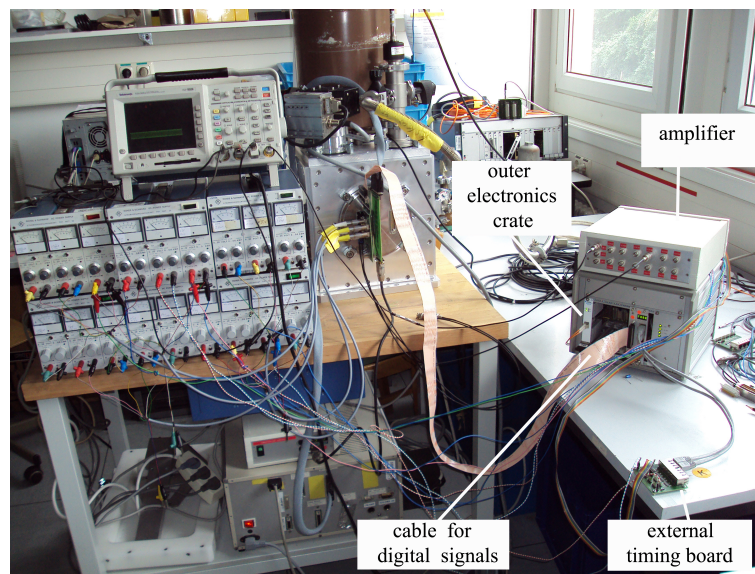


Figure 24: The whole ring of readout system

4.3 Temperature control

Temperature measurement and control is an important part in the CCD operation. In Figure 18 the inner temperature distribution board (9) is shown. It distributes signals from the temperature sensors, which can be displayed on a PC screen by using a LABVIEW data acquisition system. The board is shown in Figure 25:



Figure 25: Inner temperature distribution board.

The inner board (9) is connected to an outer temperature distribution board (see Fig. 29) outside the vacuum cryostat by a 50 pin vacuum feedthrough (see

Fig. 18). The outer board is connected to the temperature controller device which is set up by commercial PT100 acquisition module (FIELDPOINT) (Fig. 27).

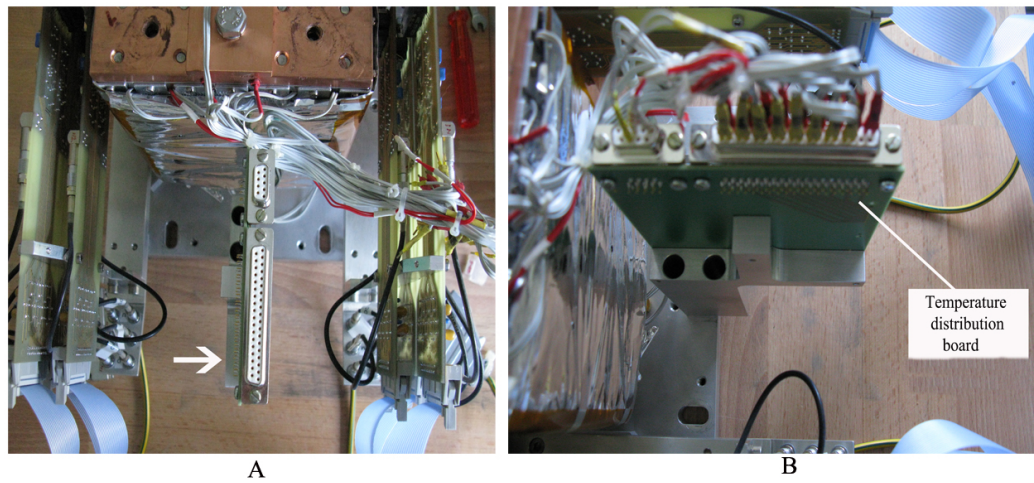


Figure 26: Installation of inner temperature distribution board (A without cabling, B with cabling). In A left and right boards are the preamplifier boards for the analog output of the CCDs.

One temperature sensor at the detector head is used for a heater feedback circuit, which keeps the detector at a predefined temperature (see Fig. 22). In our case this level is -97°C , which takes into account an offset of 3°C , i.e., temperature is about -100°C .

Figure 26 shows the installed inner temperature distribution board. (A without cabling and B with cabling to the PT100 sensors).

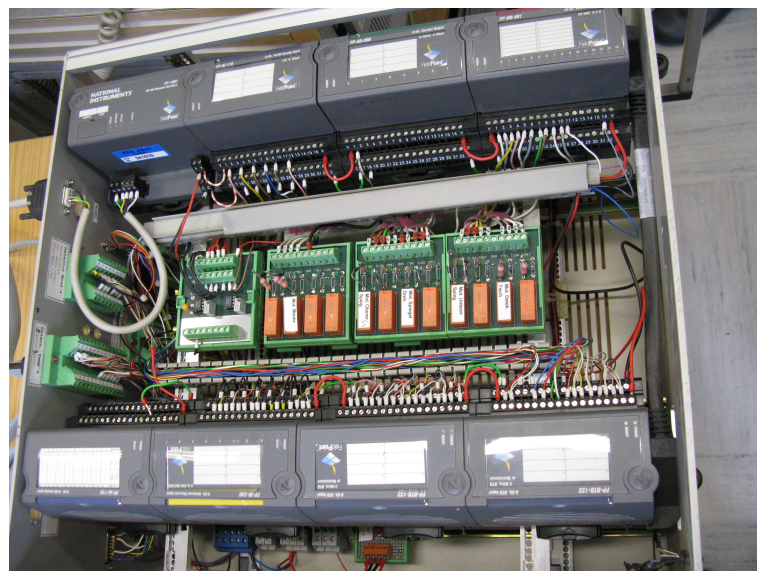


Figure 27: Temperature monitoring FIELDPOINT DAQ system.

Basically 2 x 9 temperature sensors are monitored, one from the left and one from the right side of detector. 1) CCD support, 2) CCD cooling, 3) support top, 4) support bottom, 5) shield cooling, 6) shield top, 7) shield bottom, 8) base (warm), 9) base (warm) (see Fig. 28). One set is used for monitoring by using LABVIEW. The detector head sensor of the other one is used for the heater circuit.

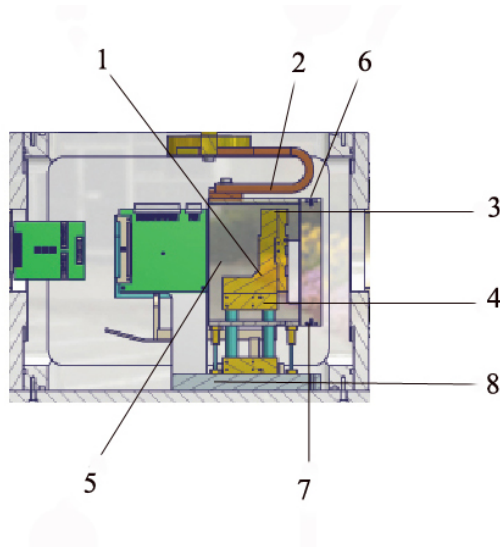


Figure 28: location of temperature sensors.

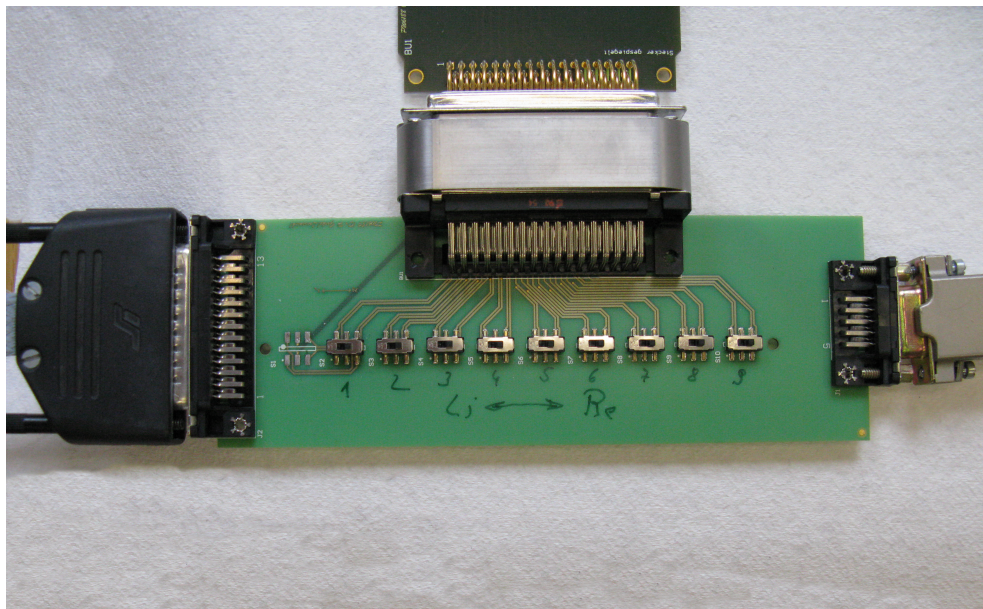


Figure 29: outer temperature distribution board.

Figure 29 shows the 50 pin vacuum connector between inner and outer temperature distribution boards, in the test setup.

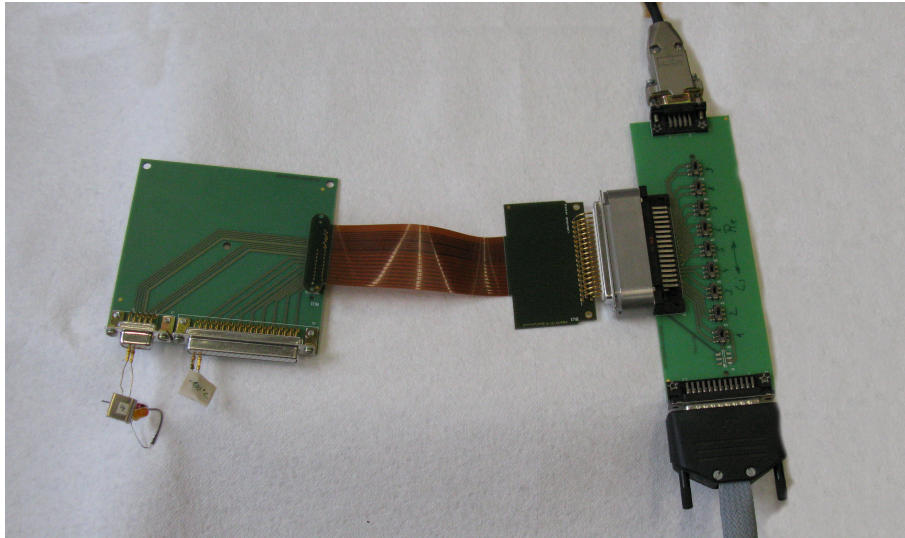


Figure 30: Test setup for the connection between inner and outer temperature distribution boards.

Temperatures are transferred to LABVIEW PC in real time. The software automatically saves/archives the temperature data for future analysis (the format is shown in Figure 33). The time interval for saving the data can be regulated manually.

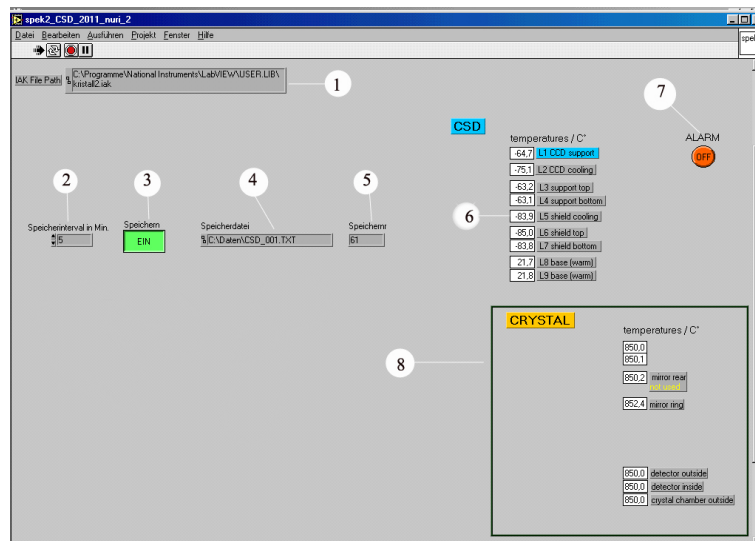


Figure 31: Screen shot of the temperature monitoring panel of LABVIEW. Crystal temperatures are not connected.

Figure 31 represents the screen shot of the temperature monitoring panel. There are multiple elements located on it:

- 1) Path to the LABVIEW program source file used in the current management.
- 2) Time interval in minutes for recording the temperature data. One can regulate this parameter by up and down arrows shown here, or just simply inserting the needed number (5 min in our case).
- 3) Start button for data recording.
- 4) Path to the data file (extension .txt).
- 5) Number of records already stored and increased automatically after each time interval defined in textbox (2).
- 6) Temperatures (L1-L9 or R1-R9). In this measurement left side set of temperature sensors was connected.
- 7) Alarm, which produces an acoustic signal if temperature L1 is outside its range (usually $-100^{\circ}\text{C} \pm 1^{\circ}\text{C}$).
- 8) Temperature monitoring panel for the Bragg crystal (not used in this measurement).

The graphical interface is made on the base of LABVIEW internal elements. The internal structure of the display panel is shown in Figurw 32:

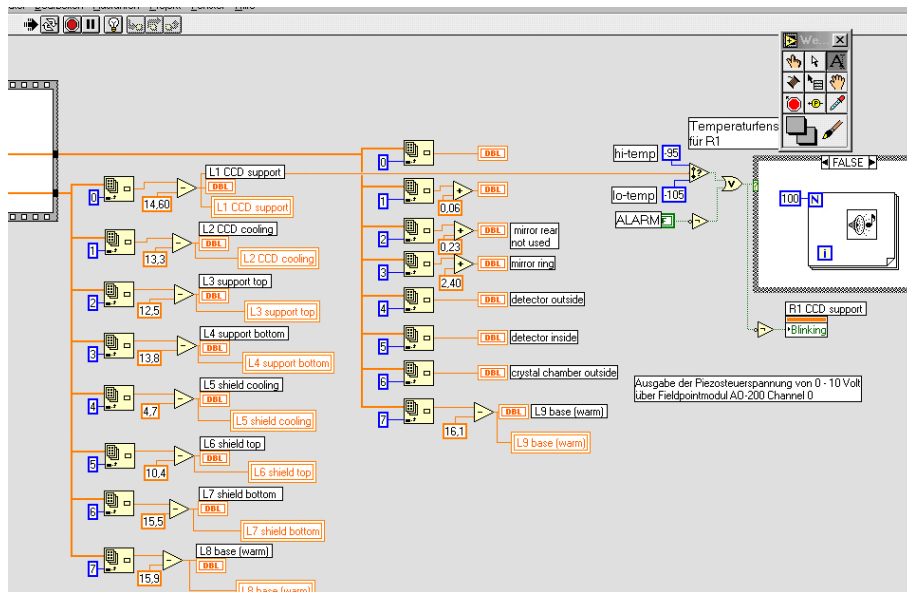


Figure 32: Internal structure of the software written in LABVIEW for data acquisition of temperature sensors.

The recorded data are kept in a txt file. The user can open it at any time to have access to the data for analysis, for drawing histograms and so on.

Nr.	Datum	Uhrzeit	L1 CCD	L2 CCD	L3 supp.	L4 supp.	L5 shield	L6.	L7.	L8.	L9.
1,00	21.04.11	11:17	24,00	24,07	24,06	24,01	24,06	24,03	24,03	24,00	23,97
2,00	21.04.11	11:23	23,98	24,05	23,94	24,00	23,79	23,95	24,00	23,98	23,96
3,00	21.04.11	11:28	23,95	23,38	23,92	24,00	20,91	22,16	23,52	23,96	23,94
4,00	21.04.11	11:33	23,79	21,65	23,84	23,92	16,34	18,31	21,48	23,93	23,93
5,00	21.04.11	11:38	23,41	19,26	23,57	23,66	11,29	13,59	18,04	23,90	23,88
6,00	21.04.11	11:43	22,72	16,60	23,10	23,21	6,37	8,67	13,76	23,85	23,83
7,00	21.04.11	11:48	21,76	13,86	22,40	22,54	1,86	3,93	9,14	23,79	23,78
8,00	21.04.11	11:53	20,57	11,18	21,50	21,66	-2,23	-0,43	4,63	23,72	23,70
9,00	21.04.11	11:58	19,18	8,56	20,40	20,59	-6,03	-4,50	0,30	23,64	23,64
10,00	21.04.11	12:03	17,62	5,98	19,13	19,32	-9,54	-8,28	-3,74	23,56	23,56
11,00	21.04.11	12:08	15,94	3,48	17,69	17,91	-12,77	-11,74	-7,52	23,48	23,48
12,00	21.04.11	12:13	14,19	1,06	16,18	16,39	-15,75	-14,95	-11,01	23,42	23,41
13,00	21.04.11	12:18	12,35	-1,27	14,55	14,77	-18,51	-17,94	-14,26	23,34	23,32
14,00	21.04.11	12:23	10,46	-3,54	12,82	13,06	-21,09	-20,70	-17,26	23,26	23,27
15,00	21.04.11	12:28	8,52	-5,74	11,05	11,26	-23,52	-23,28	-20,06	23,18	23,19
16,00	21.04.11	12:33	6,62	-7,87	9,21	9,45	-25,75	-25,68	-22,64	23,12	23,11
17,00	21.04.11	12:38	4,64	-9,97	7,35	7,58	-27,91	-27,96	-25,09	23,04	23,04
18,00	21.04.11	12:43	2,69	-12,02	5,48	5,70	-29,93	-30,12	-27,40	22,96	22,96
19,00	21.04.11	12:48	0,74	-13,99	3,59	3,81	-31,85	-32,14	-29,57	22,89	22,90
20,00	21.04.11	12:53	-1,20	-15,96	1,65	1,87	-33,71	-34,09	-31,62	22,83	22,84
21,00	21.04.11	12:58	-3,14	-17,86	-0,27	-0,05	-35,49	-35,94	-33,57	22,76	22,77
22,00	21.04.11	13:03	-5,06	-19,74	-2,18	-1,97	-37,19	-37,72	-35,43	22,70	22,72
23,00	21.04.11	13:08	-6,97	-21,57	-4,10	-3,90	-38,86	-39,41	-37,21	22,65	22,66
24,00	21.04.11	13:13	-8,88	-23,39	-6,02	-5,80	-40,46	-41,06	-38,94	22,59	22,61
25,00	21.04.11	13:18	-10,75	-25,17	-7,92	-7,71	-42,01	-42,68	-40,60	22,54	22,56
26,00	21.04.11	13:23	-12,59	-26,93	-9,79	-9,60	-43,53	-44,22	-42,24	22,49	22,52
27,00	21.04.11	13:28	-14,44	-28,66	-11,63	-11,46	-45,01	-45,77	-43,81	22,46	22,47
28,00	21.04.11	13:33	-16,23	-30,36	-13,46	-13,30	-46,47	-47,26	-45,35	22,41	22,42
29,00	21.04.11	13:38	-18,03	-32,04	-15,29	-15,10	-47,88	-48,71	-46,87	22,36	22,39
30,00	21.04.11	13:43	-19,79	-33,69	-17,10	-16,91	-49,29	-50,15	-48,33	22,31	22,34
31,00	21.04.11	13:48	-21,54	-35,31	-18,86	-18,68	-50,68	-51,53	-49,77	22,30	22,32
32,00	21.04.11	13:53	-23,25	-36,90	-20,62	-20,46	-52,01	-52,89	-51,18	22,27	22,29
33,00	21.04.11	13:58	-24,95	-38,47	-22,35	-22,19	-53,32	-54,23	-52,56	22,22	22,26
34,00	21.04.11	14:03	-26,61	-40,04	-24,03	-23,91	-54,64	-55,56	-53,93	22,20	22,24
35,00	21.04.11	14:08	-28,25	-41,56	-25,73	-25,59	-55,90	-56,86	-55,25	22,17	22,23
36,00	21.04.11	14:13	-29,88	-43,07	-27,41	-27,27	-57,19	-58,14	-56,55	22,15	22,19
37,00	21.04.11	14:18	-31,50	-44,56	-29,03	-28,91	-58,40	-59,39	-57,83	22,14	22,18
38,00	21.04.11	14:23	-33,09	-46,01	-30,68	-30,56	-59,62	-60,63	-59,06	22,11	22,18
39,00	21.04.11	14:28	-34,66	-47,49	-32,32	-32,17	-60,82	-61,84	-60,30	22,09	22,13
40,00	21.04.11	14:33	-36,21	-48,91	-33,90	-33,76	-62,01	-63,05	-61,51	22,06	22,11
41,00	21.04.11	14:38	-37,73	-50,31	-35,46	-35,33	-63,16	-64,18	-62,73	22,06	22,08
42,00	21.04.11	14:43	-39,22	-51,69	-37,00	-36,89	-64,28	-65,35	-63,90	22,01	22,07
43,00	21.04.11	14:48	-40,70	-53,05	-38,52	-38,41	-65,42	-66,47	-65,05	21,99	22,03
44,00	21.04.11	14:53	-42,17	-54,39	-40,02	-39,91	-66,54	-67,61	-66,21	21,96	22,03
45,00	21.04.11	14:58	-43,61	-55,71	-41,48	-41,37	-67,63	-68,72	-67,33	21,96	21,99
46,00	21.04.11	15:03	-45,02	-57,01	-42,94	-42,85	-68,71	-69,81	-68,45	21,93	21,97
47,00	21.04.11	15:08	-46,45	-58,30	-44,40	-44,29	-69,78	-70,88	-69,56	21,90	21,97

Figure 33: data file written by using LABVIEW, saving the temperature data.

4.4 CCD22 architecture

Standard CCDs are depleted to less than $5\ \mu\text{m}$ and, consequently, sensitive to X-rays only in $0.1 - 10\ \text{keV}$ energy range. They have very poor QE at low energies (due to absorption in the electrode structure) and at high energies (due to limited depletion depth). CCD22s have been developed for X-ray detection and to overcome these limitations.

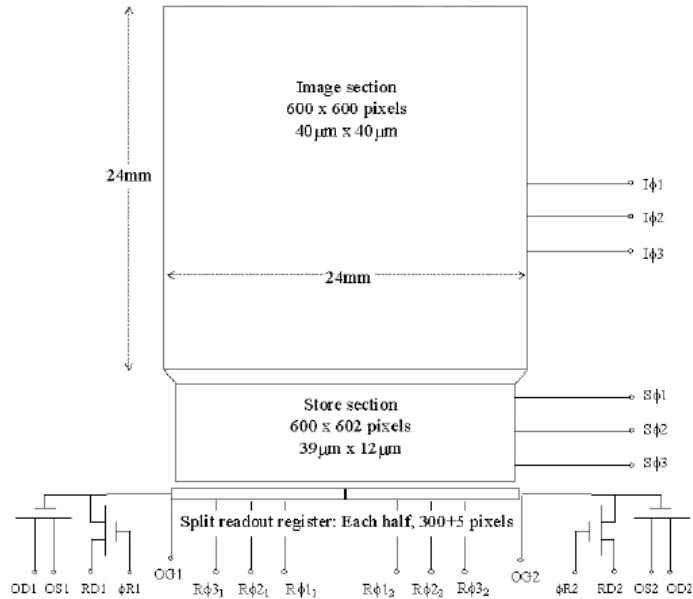


Figure 34: CCD22 device schematic.

The normal functioning of a CCD, can be divided into two phases: exposure and readout. During the first phase, the CCD passively collects the charge from incoming photons. After the exposure time is passed, the pixels are read out one line at a time.

During the readout phase, charge collected in pixels is shifted down the entire area of the CCD. While they are shifted, pixels continue to collect photons. Thus, if the shifting is not fast enough, errors can result from photons that fall on a pixel during the transfer. These errors are referred to as "vertical smearing" of impact points. and cause a source to create a vertical line above and below its exact location. Unfortunately, a faster shifting requires a faster readout leading to a marginal resolution of the detected charge.

With a frame transfer CCD one can largely overcome the vertical smearing. They are developed for high efficiency and correctness. In addition to the image area such CCDs have a storage area containing as many pixels as the image area. When imaging photons, it is usual for the store region of the device to be covered with an opaque material to prevent photon detection during readout, which again leads to smearing of the image. When the exposure time is up, charge in the image

region is transferred very rapidly to the storage area. Here, they can be read out at any speed one deems necessary to correctly measure the pixels' charge. Therefore images from frame transfer CCDs are very sharp.

The CCD22 operation can be divided into three parts: image integration, frame transfer and store region read out. This type of CCD consists of 600×600 $40 \mu\text{m}$ square pixels in the **image region**. The store region has 600×602 pixels, but these are not square and allow the **store section** to be reduced in size, making a more compact CCD. The **serial register** is split with one read-out node at either end. Charge can be clocked out of either node or both nodes simultaneously, depending upon clocking operation [20].

To maximize the high energy QE, the CCD22 is manufactured using $80 \mu\text{m}$ epitaxial, high-resistivity silicon ($4000\Omega \text{ cm}$). With the gate potential applied, a depletion depth of $30 - 40 \mu\text{m}$ is achieved with a corresponding field free depth of $40 - 50 \mu\text{m}$. The total thickness of the CCD is $350 \mu\text{m}$.

4.5 Detector operation overview

The operation of CCDs, in contrast with many other (X-ray) detectors, requires a large number of control signals and bias voltages. These include clock signals for the various sections of the device and a number of different voltage sources for correct biasing of the detector. In addition, low noise operation is required, which in turn needs low noise electronics to drive the CCD and the application of signal processing techniques to remove inherent detector noise.

Electronic circuits provide the bias voltages and a clock-sequencing device generates the clocking signals (Fig. 24). The clock signals are then level-shifted to adjust the amplitude necessary for charge transfer. The CCD output is amplified and passed through a signal processor. Finally the output signal is digitized using an analog-to-digital converter (ADC) and stored on a computer.

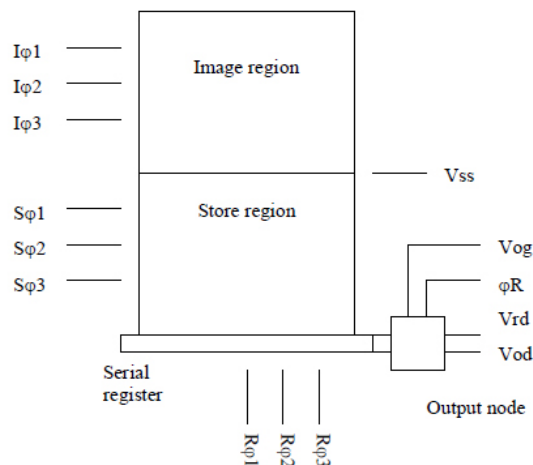


Figure 35: Typical clock and bias voltage requirements for a frame-transfer CCD.

A CCD is essentially a CMOS integrated circuit comprising a large number of metal-oxide-semiconductor capacitors and an output amplifier. The capacitor-type structures facilitate charge storage and transfer, whilst the output amplifier provides charge to voltage conversion. Figure 35 shows typical clock and bias-voltage requirements for a 3-phase frame-transfer CCD. A detailed description of these signals is given in chapter 5.

The final set of optimised CCD operating voltages are shown in Table 1. Compatibility between different devices is very good and even the output drain voltages are the same for each CCD [20].

purpose voltage	indication	optimised value (V)
Image clock	$I\varphi1, I\varphi2, I\varphi3$	3.5
Store clock	$S\varphi1, S\varphi2, S\varphi3$	7.5
Serial clock	$R\varphi1, R\varphi2, R\varphi3$	13
Reset pulse	$\varphi R,$	9.5
First output drain	1 Vod	20
Second output drain	2 Vod	20
Third output drain	3 Vod	20
Output gate	Vog	1.9
Guard ring	Vgr	20
Substrate	Vss	1.5
input drain	Vid	16.8
reset drain	Vrd	15.3
common collector voltage	Vcc	5

Table 1: CCD optimised operating voltages.

5 CCD readout and clock sequencing

In a CCD, the pixels are defined in horizontal direction by the electrode structures and in vertical direction by the channel stops (Fig. 36).

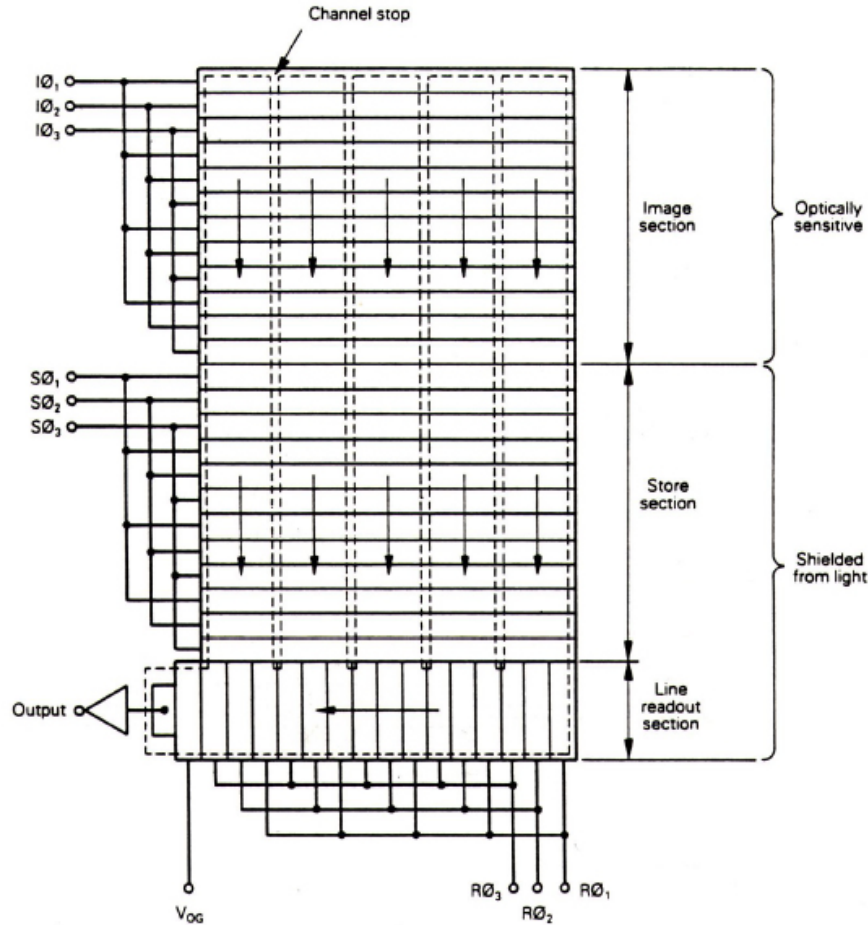


Figure 36: Typical 3 phase, frame-transfer CCD schematic. (From [15]).

In a frame-transfer device, this format is used to create an image region and a store region of pixels, where the pixels in any row are linked by a common electrode structure but divided by the perpendicular channel stops. At the base of the store region, a line readout section or serial register is created. The electrodes in this register are arranged at right angles to, and to coincide with, the pixel structure of the rows in the store region. A single row of pixels may be transferred from the store region into the serial register, and then clocked, one pixel at a time, into the output node of the CCD.

The operation of a frame-transfer CCD can be divided into three parts: image integration, frame transfer and store region read out. For simplicity and convenience we call image area signals $I\varphi_1$, $I\varphi_2$, $I\varphi_3$, storage area signals $S\varphi_1$, $S\varphi_2$, $S\varphi_3$ and readout section signals φR (*reset*), $R\varphi_1$, $R\varphi_2$ and $R\varphi_3$, correspondingly.

5.1 Image integration

Image integration is the exposure time of the image section to the source, prior to transfer of the image section charge into the store section. Integration usually occurs with a single electrode energised, typically phase 2 in a 3-phase device.

5.2 Frame transfer

Once the desired integration time is achieved, a frame transfer operation is performed to transfer charge from the image section to the store section. The image and store section clocks are operated simultaneously in the order shown in Figure 37. Timing sequence for frame transfer clock generation can be seen in Appendix A, between lines 39 and 62. Once this operation is complete integration in the image section can begin again.

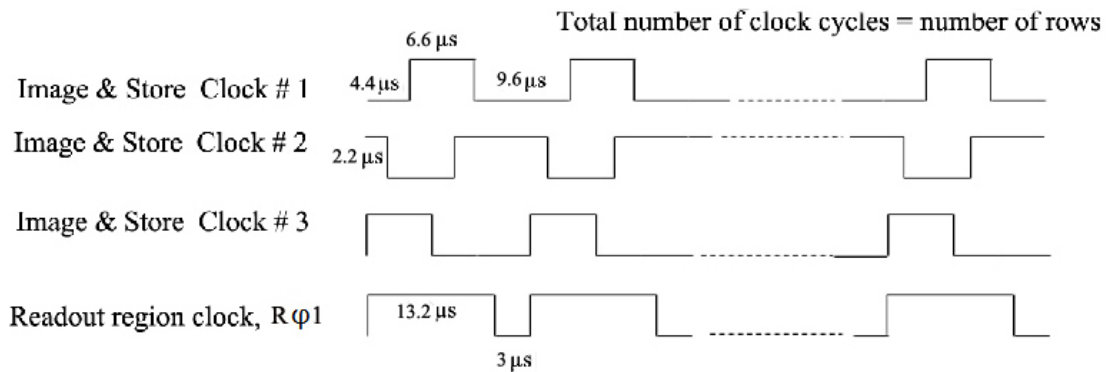


Figure 37: Frame transfer clock operation.

In this figure the total number of clock cycles corresponds to the number of CCD rows. In our case, the CCD store region has 602 rows (Fig. 34). In image and storage section we have 4 separate clocks, in both sections they have the same parameters (width and delays) and the same shape, that's why they are shown in the same figure. As can be seen from Figure 37 first comes clock 3 and $R\phi 1$, which is the first timing pulse for serial register readout, then after 2.2 μs delay comes clock 2 and after 4.4 μs clock 1. Width and delay for image and store clocks 1, 2 and 3 are the same and 6.6 μs width and 9.6 μs delay, correspondingly. The width for R1 is 13.2 μs followed by a delay of 3 μs.

The software code used to generate clock patterns for image to storage region transfer is given in Appendix A between lines 39 and 65.

One row transfer from image to storage region needs 16.2 μs, leading to 9.7 ms for the whole image region (602 rows).

5.3 Store region read-out

After frame transfer, the charge in the store section is transferred one row at a time into the serial register by performing a single cycle of the store section clocks only (see software code in Appendix A between lines 66 and 82). The charge in the serial register is then transferred one pixel at a time onto the output node of the CCD. The clock pattern to perform this operation is shown in Figure 38. The timing sequence to generate this pattern generation can be seen in Appendix A between lines 83 and 120. The read-out of charge from a single row of the

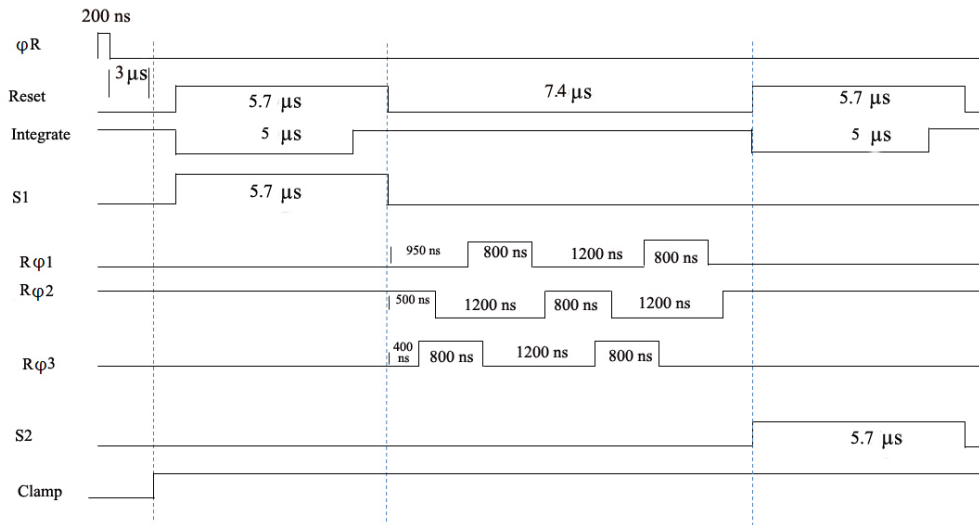


Figure 38: CCD output clock pattern.

store section of the CCD proceeds as follows. A single cycle of store section clocks transfers the charge from the final row of the store section into the serial register (Figure 37). The following sequence, illustrated in Fig. 38, is then repeated for each pixel in the serial register, equivalent to the number of pixels in the readout register (in our case 610) of the CCD.

The output node of the CCD is reset by pulsing the Reset pulse (ϕR) with a width of 200 ns. After 3 μs delay Reset, Integrate and S1 (sampling 1) pulses come together. They lead the readout region pulses, which are indicated as R ϕ 1, R ϕ 2 and R ϕ 3. These are 3 type of clocks which are essential for serial register readout. R ϕ 3 is set after 400 ns delay from the end of S1 pulse, then R ϕ 2 and R ϕ 1 are set.

Reset and Integrate pulses occur again after 7.4 μs delay from the time they appeared firstly. S2 (sampling 2) pulse comes in parallel with them and finally the Clamp pulse level goes down. The clamp pulse is up during the whole readout cycle. Widths and delays for all of the pulses are indicated in Figure 38. Reset, integrate, clamp and sampling signals are used for CCD output amplification.

Software code for readout region clocks generation is given in Appendix A between lines 83 and 121.

One line shifting time of the storage region takes $16.2 \mu s$, one pixel readout time from the serial register is $22 \mu s$. This means that $610 \times 22 \mu s = 13.420 ms$ are needed to readout one line from serial register, leading to $13.436 ms$ for one line shifting and readout. This means $8.088 s$ for whole store region shift and readout. If we add image to storage region transfer time to this value, we receive 8.097 seconds for the entire CCD readout.

5.4 Readout scheme

The data from CCDs read out is based on C programming language. Timing sequences for readout operation are generated by a software program. The source code is shown in Appendix A.

The source file for timing is compiled on the linux based PC and through the fiber optic connection uploaded to the SRAM memory of sequencer, which is located in front-end electronics crate. The size of SRAM is 524288×72 bit words. Per word 64 and 8 bits are used as data and control bits respectively. The timing sequence is written in memory as bit patterns. Every bitline corresponds to a specific pin number on the sequencer output. According to this it's important to know which signals use which bits, otherwise they can't be transmitted correctly to CCDs. The control unit, which acts as a processor for the sequencer makes decisions based on the content of the SRAM. According to this directives, the control unit takes appropriate data from SRAM and transfers it to the FIFO (first-in-first-out) module. The output FIFO is readout with $100 MHz$, i.e., output signals appear in a $10 ns$ sequence.

From here digital pulses, which are used to readout the information from CCDs, are transferred to the outer distribution board (Fig. 23) through the 64 wire cable. The memory bit to pin correspondence can be seen in Table 4 of Appendix B. Power supplies provide all needed voltages (see Table 1), and together with the digital signals are transferred to the CCDs through the 50 pin vacuum fieldthrough connector of the outer distribution board (see Fig. 24). Such connector is shown in Figure 30 before welded in the flange of the cryostat. Table 5 in Appendix B shows signal to pin correspondence on this connector.

In our case, at the same time readout is done from only one half of array of CCDs (i.e. 3CCDs). Signals are preliminarily generated to readout 6 CCDs, so if we plug the outer distribution board in another connector on vacuum cryostat we can read from the second half of array.

The analog output received from preamplifiers has a low level ($\approx 35 meV$ for $6 keV$ X-rays) and needs to be further amplified. For this reason they enter an amplifier device. Digital pulses needed to synchronise the amplification procedure are sent from the sequencer to external timing board, which distributes them to amplifier device (see Fig. 24). Amplifier has two functions, it amplifies the input signals and subtracts noise level from them. This means sampling the noise level, then sampling the signal together with noise. Subtraction gives the real signal level. Resulting signals enter ADC unit and are digitized.

5.5 How the sequencer timing is generated

General routines for timing (for instance generation of pulses and delays, jumps to another routines, current memory address calculation, trigger signal setting and so on) are preliminarily defined in a source file, which can be freely used as an instrument to create complex timing sequences (see Appendix A).

There main routines for timing generation are explained below:

Routine for pulse generation is written in this way

$$\textit{MakePuls} (\textit{bit}, \textit{start_address}, \textit{width}), \quad (18)$$

arguments are memory bitline definition, address in memory, where pulse must start and pulse width in nanoseconds. Address is linked to time, because the output signal appears in 10 ns sequence, the exact starting time must be defined for every pulse. To calculate current address in memory, where the next pulse can be started following command is used:

$$\textit{current_address}; \quad (19)$$

The result of this command can be assigned to variable, in order to use it as starting address for other pulses. For example, the following command

$$\textit{MakePuls} (25, \textit{current_address}, 200), \quad (20)$$

generates the pulse at bitline 25, with the width of 200 ns and the *current_address* already points the end of this pulse. So if the command (20) is repeated, the pulse will be set at the end of previous one. If in the beginning the result of *current_address* command is assigned to variable and then used in commands as argument, pulses can be started at the same time. So, this command is effective to define the correct timing sequence.

Delays for pulses are generated the same way, but the name of command is different:

$$\textit{MakeDelay} (\textit{bit}, \textit{start_address}, \textit{delay}), \quad (21)$$

The *JSR*(jump to subroutine) command is used to go to specific routine. Argument for this command is the name of the routine. For example command *JSR* (“*image*“) finds the routine named (“*image*“) in SRAM memory and transfers to FIFO. The *RTS* command is used to return back from FIFO to SRAM. Command *Loop* has one argument in addition, which indicates how often the routine is performed. For example, *Loop* (“*image*“), 3) performs the routine named “*image*“ 3 times.

The command *NANO2BIT* is used to convert nanoseconds to bits.

BIT2NANO acts vice versa. The command *SetTriggOut* is used to set the trigger for timing.

5.6 ADC format for data digitization

In our case, 14 bit ADCs are used, which means that the maximum of the digitized value is $2^{14} = 16384$. The ADC unit has 4 inputs, but as mentioned in our case only one half of the array of CCDs (i.e., 3 CCDs) were physically connected to it. The digitized data are written in a binary file according to specific format. 8 frames are written per file, where one frame corresponds to one readout of a CCD. Each file consists of header containing information about current date and time, frame number, given as 3 integer values of 32 bit length followed by the CCD data.

The contents of four ADC units is stored in two 32 bit integer values, where one ADC is matched to one short (16 bits) value (see Fig. 39). In our case, the fourth ADC unit is unused and CCD1, CCD2 and CCD3 are connected to ADC0, ADC1 and ADC2 respectively.

One integer of CCD data contains information about one pixel from two CCDs. The first 16 bits correspond to the first pixel of the first CCD, second 16 bits to first pixel of the second one. Subsequent integer contains the value for first pixel of the third and fourth CCDs correspondingly. As one CCD contains 602×610 pixel, the data part of one frame contains $602 \times 610 \times 2$ integer values.

5.7 ADC binary file readout

The binary file is processed by a program written in C programming language to generate spectra of the individual CCDs in ASCII format. The data words are decomposed and stored as 16 bit spectra in the format $(n_1 n_2 n_3 n_4 n_5)$, where n_1 is channel number(1-16384) and the other columns correspond to ADC values.

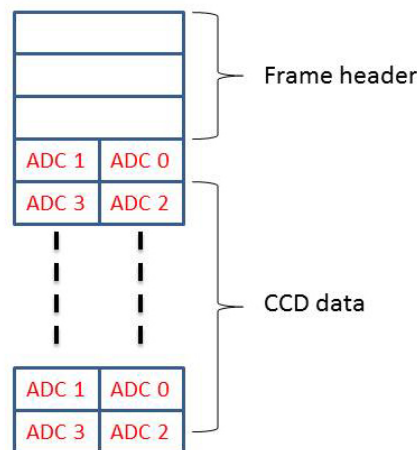


Figure 39: Data format of CCD readout.

5.8 Results

In order to test the response of the CCDs, a measurement using a radioactive source has been performed. As radioactive source ^{55}Fe is used, which produces Mn X-rays. The energies of $K\alpha$ and $K\beta$ are 5892 eV and 6490 eV, respectively. The ratio of their intensity is expected to about 7.2 [25].

Based on the data received from each CCD, an energy spectrum plot is generated. For plotting we use freeware software product called ‘‘Gnuplot’’. The experiment revealed that CCD2 is damaged, so results can be presented here only for CCD1 and CCD3.

The CCD output is done under three conditions: 1) Source is at 10 cm distance from CCD detector sensitive surface (at the Beryllium window) 2) 20 cm distance, i.e., 10 cm before the Be window, and 3) without source.

In order to improve statistics, the measurements are done six times for each condition and each CCD, i.e., 48 frames per CCD were recorded. The results of the six measurements are summed up.

Position \bar{x} , uncertainty of the position $\Delta\bar{x}$ and widths Δx of $K\alpha$ and $K\beta$ lines were estimated by standard formulas of statistics

$$\bar{x} = \frac{\sum ch_i \cdot n_i}{\sum n_i}. \quad (22)$$

Here ch_i is number of the ADC channel and n_i is the number of counts in this channel.

$$\Delta\bar{x} = \frac{\Delta x}{\sqrt{2 \cdot n}}, \quad (23)$$

where $n = \sum n_i$ and

$$\Delta x = \sqrt{\frac{\sum (ch_i - \bar{x})^2}{(n - 1)}}. \quad (24)$$

The parameter full width half maximum (FWHM) represents the resolution of charge of the CCD:

$$FWHM = 2.355 \cdot \Delta x. \quad (25)$$

The results are shown in Table 2.

Figure 40 shows energy spectra for CCD1 and CCD3 when the source is at 10 cm distance from the detector’s sensitive surface. The energy runs from right to left because of the negative polarity of the signal which is added to a positive offset before digitization.

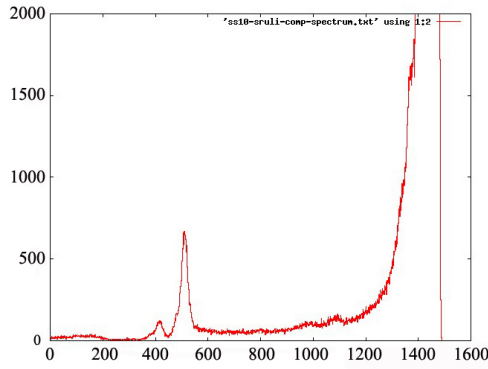
As can be seen from the energy spectrum of the CCD1 (Fig. 40), the noise peak is at channel 1457, the peak for $K\alpha$ is at 510 and for $K\beta$ at 408. The energy corresponding to the noise peak is assumed to be at 0 eV because the noise level has been subtracted by the amplifier circuit using correlated double sampling. The $K\alpha$ energy must be at 5892 eV. If we subtract the channel of the peak of $K\alpha$ from the channel of the noise peak, we get the number of channels corresponding to an energy interval of 5892 eV, i.e., we know the energy E_{ch} corresponding to one channel. From here we can calculate, that the position of the $K\beta$ is expected at

6527 eV. The results are in reasonable agreement with the expected value of 6490 eV. The same procedure is performed for CCD3.

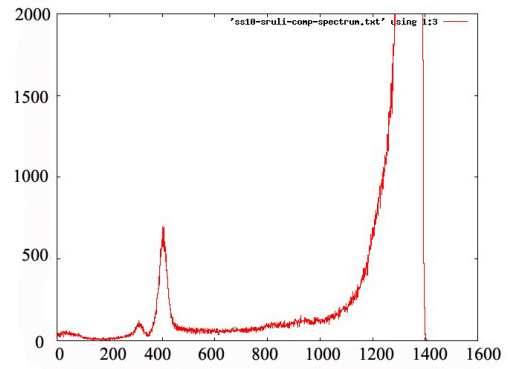
In this way we can predict energy values for the $K\beta$ for all measuring conditions. The results are given in Table 3.

	CCD1			CCD3		
	$K\alpha$	$K\beta$	noise	$K\alpha$	$K\beta$	noise
Distance to source = 10cm						
\bar{x}	510	408	1457	403	305	1355
Δx	14.6	14.6	11.2	16.0	16.0	13.1
$\Delta\bar{x}$	0.1	0.2	0.002	0.1	0.2	0.002
FWHM	34.4±0.3	34.4±0.3	26±0.004	37.75±0.29	37.75±0.29	31±0.005
Integral	19668	2656	17272306	22281	2186	17235869
Distance to source = 20cm						
\bar{x}	504	407	1452	397	307	1350
Δx	16.12	16.12	11.26	16.92	16.92	12.92
$\Delta\bar{x}$	0.2	0.5	0.002	0.2	0.5	0.002
FWHM	37.9±0.6	37.9±0.6	27±0.004	39.77±0.56	39.77±0.56	30.4±0.005
Integral	4558	551	17436488	5003	644	17445458
Without source						
\bar{x}	0	0	1464	0	0	1361
Δx	0	0	5.19	0	0	9.4
$\Delta\bar{x}$	0	0	0.001	0	0	0.001
FWHM	0	0	12±0.002	0	0	22±0.004
Integral	0	0	17493278	0	0	17528711

Table 2: parameters of energy spectra of the ^{55}Fe radioactive source.

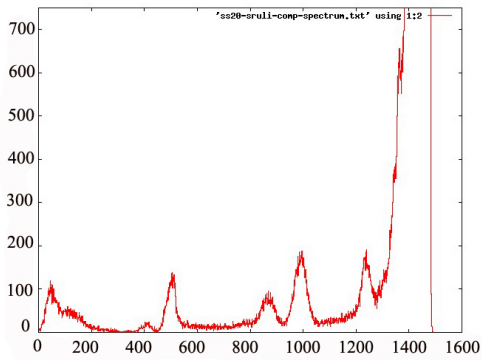


CCD 1

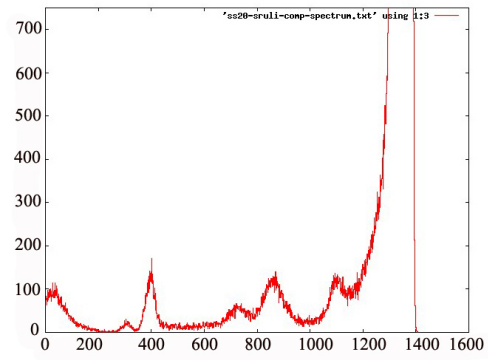


CCD 3

Figure 40: energy spectrum for CCD1 and CCD3 when the source ^{55}Fe is at 10 cm distance from the detector's sensitive surface.



CCD 1



CCD 3

Figure 41: energy spectrum for CCD1 and CCD3 when the source ^{55}Fe is at 20 cm distance from the detector's sensitive surface.

Corresponding energy calibration plots are shown in Figure 43 and 44.

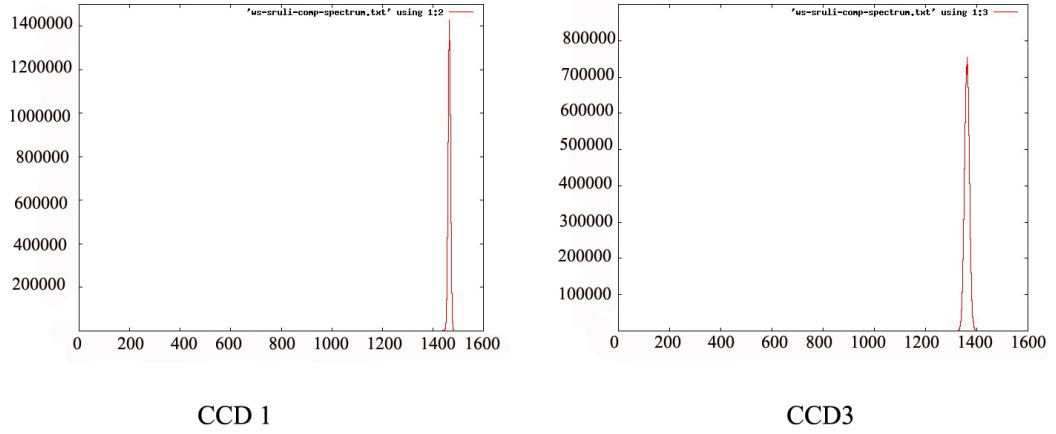


Figure 42: energy spectrum for CCD1 and CCD3 without ^{55}Fe .

	CCD1	CCD3
Distance to source = 10cm		
$K\alpha$	5892 eV	5892 eV
$K\beta$	6527 eV	6500 eV
$\frac{K\alpha}{K\beta}$	7.3	10.2
E_{ch}	6.222 eV/ch	6.190 eV/ch
Distance to source = 20cm		
$K\alpha$	5892 eV	5892 eV
$K\beta$	6495 eV	6448 eV
$\frac{K\alpha}{K\beta}$	8.27	7.8
E_{ch}	6.215 eV/ch	6.183 eV/ch

Table 3: Energies for $K\alpha$ (input) and $K\beta$ (prediction).

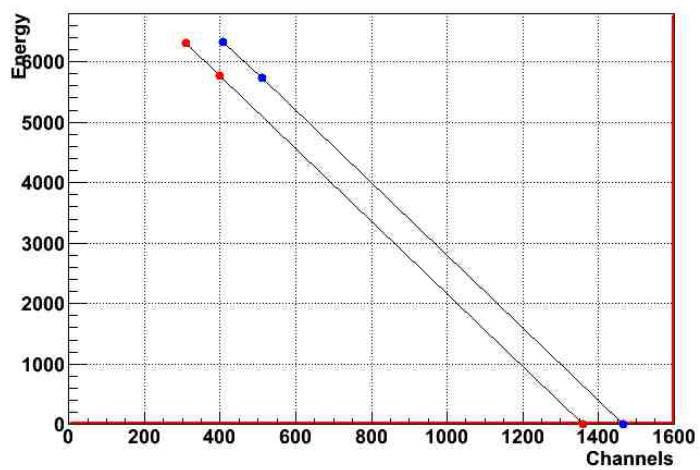


Figure 43: energy calibration for CCD1 and CCD3 when the source ^{55}Fe is at 10 cm distance from the detector's sensitive surface.

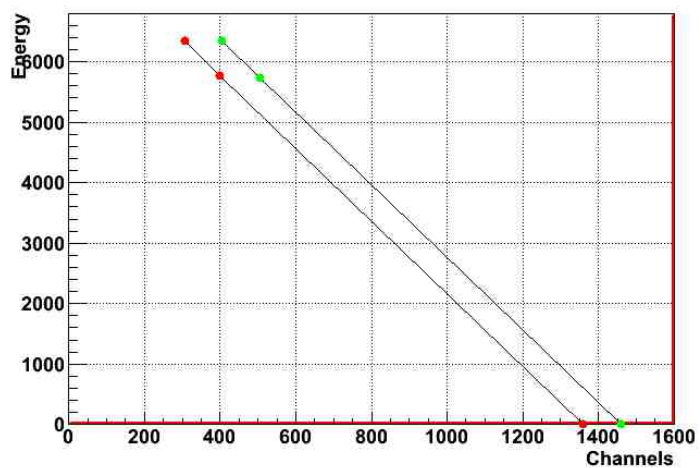


Figure 44: energy calibration for CCD1 and CCD3 when the source ^{55}Fe is at 20 cm distance from the detector's sensitive surface.

6 Conclusion

The new readout structure for the MOS-type CCD array has been successfully adapted from a system used for fully depleted fast CCDs. It will allow a high level of flexibility and guarantees a significantly enhanced reliability compared to the previously used system based on a PC operated under Windows Visual Basic.

The new system produces timing sequences simultaneously for all six CCDs leading to no need for multiplexing and thus accelerates the readout by a factor of three. The next step to be done is optimisation of operating parameters which in addition improves the whole system working efficiency.

A Program Code to generate the timing sequence for the readout operation

```
1  Description()
2
3  {
4
5  Extra-Args:
6  float exposureTime = .1;  //  ! msec!!
7  int IS_width = 2200;
8  int IS_delay = 3000;
9  int pixels_in_row = 602;
10 int pixels_in_column = 610;
11 Comment:
12     First try;
13 }
14
15
16 int L_PHI_1[2] = {14, 30};
17 int L_PHI_2[2] = {15, 31};    //!  INVERTED !!!
18 int L_PHI_3[2] = {0, 16} ;
19
20 int S_PHI_1[2] = {1, 17};
21 int S_PHI_2[2] = {2, 18};    //!  INVERTED !!!
22 int S_PHI_3[2] = {3, 19};
23 int R_PHI_1[2] = {4, 20};
24 int R_PHI_2[2] = {4, 20};    //!  INVERTED !!!
25 int R_PHI_3[2] = {6, 22};
26 int PHI_R[2] = {7, 23};
27
28 int RESET = 33;
29 int S1 = 37;
30 int S2 = 38;
31 int INTGATE = 39;    //!  INVERTED !!!
32
33 int GAIN1 = 32;    //!  INVERTED !!!
34 int SEL = 34;
35 int CLamp = 35;
36 int GAIN0 = 36;    //!  INVERTED !!!
37
38
39     SEQfifo from_image_to_storage(int w, int d)
40     {
41
42 //! Image and storage region signals working simultaneously
43
```

```

44 int j, i, s;
45
46 s = CURRENT_ADDR;
47
48 for (i = 0; i < 2; i++) {
49 j = MakePuls(L_PHI_3[i], s, 3 * w);
50 j = MakeDelay(L_PHI_2[i], s, w);
51 MakePuls(L_PHI_2[i], j, 3 * w);
52 j = MakeDelay(L_PHI_1[i], s, 2 * w);
53 MakePuls(L_PHI_1[i], j, 3 * w);
54
55 j = MakePuls(S_PHI_3[i], s, 3 * w);
56 j = MakeDelay(S_PHI_2[i], s, w);
57 MakePuls(S_PHI_2[i], j, 3 * w);
58 j = MakeDelay(S_PHI_1[i], s, 2 * w);
59 MakePuls(S_PHI_1[i], j, 3 * w);
60
61 j = MakePuls(R_PHI_1[i], s, 6 * w);
62 MakeDelay(R_PHI_1[i], j, d);
63
64 }
65 }
66 SEQfifo store_region(int w, int d)
67 {
68
69 //! storage region signals
70 int j, i, s;
71 s = CURRENT_ADDR;
72 for (i = 0; i < 2; i++) {
73 j = MakePuls(S_PHI_3[i], s, 3 * w);
74 j = MakeDelay(S_PHI_2[i], s, w);
75 MakePuls(S_PHI_2[i], j, 3 * w);
76 j = MakeDelay(S_PHI_1[i], s, 2 * w);
77 MakePuls(S_PHI_1[i], j, 3 * w);
78
79 j = MakePuls(R_PHI_1[i], s, 6 * w);
80 MakeDelay(R_PHI_1[i], j, d);
81 }
82 }
83 SEQfifo readout_line(int clamp Delay, int w, int d)
84 {
85 //! Readout region signals
86 int clampStart;
87 int phiStart;
88 int j, i, s;
89
90 s = CURRENT_ADDR;

```

```

91     for (i = 0; i < 2; i++) {
92         j = MakePuls(PHI_R[i], s, 200);
93         clampStart = MakeDelay(PHI_R[i], j, clampDelay - 200);
94     }
95
96     phiStart = MakePuls(RESET, clampStart+NANO2BIT(100), 5700);
97     phiStart += NANO2BIT(400);
98     MakePuls(INTGATE, clampStart+NANO2BIT(100), 5000);
99     MakePuls(S1, clampStart+NANO2BIT(100), 5700);
100    for (i = 0; i < 2; i++)
101    {
102        j = MakePuls(R_PHI_3[i], phiStart, w);
103        j = MakeDelay(R_PHI_3[i], j, d);
104        MakePuls(R_PHI_3[i], j, w);
105
106        j = MakeDelay(R_PHI_2[i], phiStart, 100);
107        j = MakePuls(R_PHI_2[i], j, d);
108        j = MakeDelay(R_PHI_2[i], j, w);
109        MakePuls(R_PHI_2[i], j, d);
110
111        j = MakeDelay(R_PHI_1[i], phiStart, 550);
112        j = MakePuls(R_PHI_1[i], j, w);
113        j = MakeDelay(R_PHI_1[i], j, d);
114        MakePuls(R_PHI_1[i], j, w);
115    }
116    MakePuls(RESET, phiStart + NANO2BIT(7000), 5700);
117    MakePuls(INTGATE, phiStart + NANO2BIT(7000), 5000);
118    j = MakePuls(S2, phiStart + NANO2BIT(7000), 5700);
119
120    MakePuls(CLamp, clampStart, BIT2NANO(j-clampStart+500));
121    }
122
123    SEQroutine transfer(void)
124
125    {
126    //! These two region signals work simultaneously in order to transfer pixels
from Image Region 127      to Store Region
128    from_image_to_storage(IS_width, IS_delay);
129    RTS;
130    }
131    SEQroutine one_row(void)
132
133    {
134    //! These Routine moves one row of Pixels from store region to Readout
region.
135    store_region(IS_width, IS_delay);

```

```

136     RTS;
137     }
138     SEQroutine readout(void)
139
140     {
141     //! These Routine reads only one pixel from the row,in Readout region.
142     readout_line(3300, 800, 1200);
143     RTS;
144     }
145     SEQroutine Read(void)
146     {
147     JSR("one_row");
148     Loop("readout", pixels_in_column);
149     RTS;
150     }
151     SEQroutine trout(void)
152     {
153     IncCounter(1);
154     StartTimer(10000.0 * exposureTime);
155     Loop("transfer",pixels_in_row);
156     SetTriggOut(3);
157     SetTriggOut(3);
158     Loop("Read",pixels_in_row);
159     RTS;
160     }
161
162     SEQmain MainLoop(void)
163     {
164     int i;
165
166     i = WhileHalt;
167     JSR("trout");
168     Jump(i-1);    //! Jump to 'WhileHalt' to close loop
169     }

```

B Relationship between digital signals, memory bits and corresponding cabling pins.

In timing software two groups of digital signals exist. Signals (1) are used to readout the left CCD column and signals (2) for the right column, respectively. The left column consists of CCD4, CCD5, CCD6 and right one of CCD1, CCD2 and CCD3, as it is shown in Fig. 22

Sinal	corresponding bit	pin number	signal	corresponding bit	pin number
$I\varphi 1$ (1)	14	10	$I\varphi 1$ (2)	30	26
$I\varphi 2$ (1)	15	9	$I\varphi 2$ (2)	31	25
$I\varphi 3$ (1)	0	8	$I\varphi 3$ (2)	16	24
$S\varphi 1$ (1)	1	7	$S\varphi 1$ (2)	17	23
$S\varphi 2$ (1)	2	6	$S\varphi 2$ (2)	18	22
$S\varphi 3$ (1)	3	5	$S\varphi 2$ (2)	19	21
$R\varphi 1$ (1)	4	4	$R\varphi 1$ (2)	20	20
$R\varphi 2$ (1)	5	3	$R\varphi 2$ (2)	21	19
$R\varphi 3$ (1)	6	2	$R\varphi 2$ (2)	22	18
φR (1)	7	1	φR (2)	23	17

Table 4: Relation between digital signals, memory bits and corresponding cabling pins.

Sinal	corresponding pin	Sinal	corresponding pin
Vid	21	Vgr	5
Vog	6	Vrd	7
Vss	8	1Vod	10
2Vod	9	3Vod	25
PA -15V	23	PA +15V	27
φR	11	$I\varphi 1$	13
$I\varphi 2$	16	$I\varphi 3$	29
$S\varphi 1$	31	$S\varphi 2$	14
$S\varphi 3$	15	$R\varphi 1$	33
$R\varphi 2$	17	$R\varphi 3$	12
GND Vid	21	GND Vgr	38
GND Vog	22	GND PA -15V	39
GND Vrd	40	GND 1Vod	26
GND 2Vod	42	GND 3Vod	41
GND PA +15V	43	GND φR	44
GND $I\varphi 1$	32, 45, 46	GND $S\varphi 1$	30, 47, 48
GND $S\varphi 1$	28, 49, 50	AN1 P	34
AN1 N	35	AN2 P	18
AN2 N	19	AN3 P	1
AN3 N	2		

Table 5: Relationship between digital signals, supply voltages and inner and outer distribution board connector pins.

As it's seen from Table 5, each signal comes with corresponding grounding signals. AN1 N, AN1 P, AN2 N, AN2 P and AN3 N, AN3 P are analog output signals from corresponding three CCDs.

References

- [1] Phys. Rev. A, “ $K\alpha$ and $K\beta$ x-ray emission spectra of metallic scandium”, 60, 2018 (1999).
- [2] Prog. Part. Nucl. Phys., “Precision spectroscopy of light exotic atoms”, D. Gotta, 52 (2004).
- [3] Thomas Strauch, Diplomarbeit, “Aufbau eines Bragg-Kristallspektrometers und Test mit Barium $L\gamma_{2,3}$ Spektren”, diploma thesis, University of Cologne (2005).
- [4] AIP conf. proc, “A compact setup of fast pnCCDs for exotic atom measurements”, eds. Y. Yamazaki and M. Wada, 793, 341 (2005).
- [5] Michael M Woolfson, “An introduction to X-ray crystallography”, Second edition, (Cambridge University Press, USA) (1997).
- [6] Eberhard Haug, Werner Nakel, “The Elementary Process of Bremsstrahlung”, (World Scientific Publishing, USA) (2004).
- [7] Von Laue, M., Ann der Physik, 41, 971, 1913.
- [8] W. L. Bragg, Proc. Cambridge Philos. Soc. 17, 43 (1913).
- [9] Agarwal, B. K., I. S., X-ray spectroscopy, first ED., 134 (1979).
- [10] A.E. Sandstrom, Handbuch der Physik, Band XXX (Springer, Berlin) 78 (1952).
- [11] W.H. Zachariasen, Theory of X-ray Diffraction in Crystals J.Wiley and Sons Inc., New York (1947).
- [12] H.H. Johann, Z. Phys. 69 (1931).
- [13] Christian Weidemann, Diplomarbeit, “Messung der chemischen Verschiebung von $K\alpha$ und $K\beta$ Übergängen in Mangan”, diploma thesis, Friedrich-Schiller-University, Jena (2007).
- [14] G. Zschornack, G.Müller and G.Musiol, Nucl. Instr. Meth. 200, 481 (1982).
- [15] James R. Janesick, “Scientific Charge-Coupled Devices” (SPIE Press, Bellingham, Washington) (2001).
- [16] Nick Nelms et al., Nucl. Instr. Meth. A 484, 419 (2002).
- [17] G. Prigozhin, K. Gendreau, M. Bautz, B. Burke, G. Ricker, Abstract “The depletion depth of high resistivity X-ray CCDs.”(1988).
- [18] P. Indelicato et al. Rev. Sci. Instr. 77 (2006) 043107.
- [19] Jerrold T. Bushberg et al., “The essential Physics of medical imaging”, (Edwards Brothers, USA) (2002).

- [20] Nicholas Nelms, “A new determination of the charged pion mass and muon neutrino mass upper limit from exotic atom X-ray spectroscopy”, PhD thesis, University of Leicester (2002).
- [21] B. R. Martin, “Nuclear and Particle Physics”, (Antony Rowe LTD, United Kingdom) (2009).
- [22] Helmuth Spieler, “Semiconductor Detector Systems”, (Oxford University Press, United Kingdom) (2005).
- [23] Dr. William R. Leo, “Techniques For Nuclear and Particle Physics Experiments”, (Springer, Berlin) (1994).
- [24] Howard Austerlitz, “Data Acquisition Techniques Using Pcs”, (Elsevier science, USA) (2003).
- [25] App. Radiat. Isot., “Half life and X-ray emission probabilities of ^{55}Fe , 53, 469 (2000).